



**HAL**  
open science

## Predicted asteroseismic detection yield for solar-like oscillating stars with PLATO

M. J. Goupil, C. Catala, R. Samadi, K. Belkacem, R. M. Ouazzani, D. R. Reese, T. Appourchaux, S. Mathur, J. Cabrera, A. Börner, et al.

► **To cite this version:**

M. J. Goupil, C. Catala, R. Samadi, K. Belkacem, R. M. Ouazzani, et al.. Predicted asteroseismic detection yield for solar-like oscillating stars with PLATO. *Astronomy and Astrophysics - A&A*, 2024, 683, pp.A78. 10.1051/0004-6361/202348111 . hal-04496846

**HAL Id: hal-04496846**

**<https://hal.science/hal-04496846>**

Submitted on 8 Mar 2024

**HAL** is a multi-disciplinary open access archive for the deposit and dissemination of scientific research documents, whether they are published or not. The documents may come from teaching and research institutions in France or abroad, or from public or private research centers.

L'archive ouverte pluridisciplinaire **HAL**, est destinée au dépôt et à la diffusion de documents scientifiques de niveau recherche, publiés ou non, émanant des établissements d'enseignement et de recherche français ou étrangers, des laboratoires publics ou privés.

# Predicted asteroseismic detection yield for solar-like oscillating stars with PLATO

M. J. Goupil<sup>1</sup>, C. Catala<sup>1</sup>, R. Samadi<sup>1</sup>, K. Belkacem<sup>1</sup>, R. M. Ouazzani<sup>1</sup>, D. R. Reese<sup>1</sup>, T. Appourchaux<sup>2</sup>, S. Mathur<sup>3,4</sup>, J. Cabrera<sup>5</sup>, A. Börner<sup>6</sup>, C. Paproth<sup>6</sup>, N. Moedas<sup>7,8</sup>, K. Verma<sup>9</sup>, Y. Lebreton<sup>1,10</sup>, M. Deal<sup>11</sup>, J. Ballot<sup>12</sup>, W. J. Chaplin<sup>13</sup>, J. Christensen-Dalsgaard<sup>14</sup>, M. Cunha<sup>7</sup>, A. F. Lanza<sup>15</sup>, A. Miglio<sup>16,17</sup>, T. Morel<sup>18</sup>, A. Serenelli<sup>19,20</sup>, B. Mosser<sup>1</sup>, O. Creevey<sup>21</sup>, A. Moya<sup>22</sup>, R. A. Garcia<sup>23</sup>, M. B. Nielsen<sup>13</sup>, and E. Hatt<sup>13</sup>

(Affiliations can be found after the references)

Received 29 September 2023 / Accepted 14 December 2023

## ABSTRACT

**Aims.** In this work, we determine the expected yield of detections of solar-like oscillations for the targets of the foreseen PLATO ESA mission. Our estimates are based on a study of the detection probability, which takes into account the properties of the target stars, using the information available in the PIC 1.1.0, including the current best estimate of the signal-to-noise ratio (S/N). The stellar samples, as defined for this mission, include those with the lowest noise level (P1 and P2 samples) and the P5 sample, which has a higher noise level. For the P1 and P2 samples, the S/N is high enough (by construction) that we can assume that the individual mode frequencies can be measured. For these stars, we estimate the expected uncertainties in mass, radius, and age due to statistical errors induced by uncertainties from the observations only.

**Methods.** We used a formulation from the literature to calculate the detection probability. We validated this formulation and the underlying assumptions with *Kepler* data. Once validated, we applied this approach to the PLATO samples. Using again *Kepler* data as a calibration set, we also derived relations to estimate the uncertainties of seismically inferred stellar mass, radius, and age. We then applied those relations to the main sequence stars with masses equal to or below  $1.2 M_{\odot}$  belonging to the PLATO P1 and P2 samples and for which we predict a positive seismic detection.

**Results.** We found that we can expect positive detections of solar-like oscillations for more than 15 000 FGK stars in one single field after a two-year observation run. Among them, 1131 main sequence stars with masses of  $\leq 1.2 M_{\odot}$  satisfy the PLATO requirements for the uncertainties of the seismically inferred stellar masses, radii, and ages. The baseline observation programme of PLATO consists of observing two fields of similar size (one in the southern hemisphere and one in the northern hemisphere) for two years apiece. Accordingly, the expected seismic yields of the mission amount to over 30 000 FGK dwarfs and subgiants, with positive detections of solar-like oscillations. This sample of expected solar-like oscillating stars is large enough to enable the PLATO mission's stellar objectives to be amply satisfied.

**Conclusions.** The PLATO mission is expected to produce a catalog sample of extremely well seismically characterized stars of a quality that is equivalent to the *Kepler* Legacy sample, but containing a number that is about 80 times greater, when observing two PLATO fields for two years apiece. These stars are a gold mine that will make it possible to make significant advances in stellar modelling.

**Key words.** asteroseismology – stars: fundamental parameters – stars: oscillations – stars: solar-type

## 1. Introduction

The PLANetary Transits and Oscillations of stars (PLATO) mission is the ESA Cosmic Vision M3 mission and its launch is scheduled for the end of 2026. Its main objectives are 1) the detection and accurate and precise characterisation of exoplanets down to Earth-size planets in the habitable zone of solar-like stars, 2) the accurate and precise determinations of the basic parameters of their host stars (mass, radius, age, etc.), and 3) careful statistical analyses of the above characteristics in order to better understand the formation and evolution of planetary and stellar systems (hereafter, stellar systems). Sufficiently precise determinations of the characteristics of these stellar systems require very high-quality photometry carried out continuously over long periods of time, hence, the need for a space mission. Furthermore, the required accuracy calls for improvements of the stellar models used to estimate the age of the star-planet system. Improving the processes of stellar modelling is thus an intrinsic main objective of the PLATO mission (Rauer et al. 2014; Rauer et al., in prep.). The science operation phase of PLATO is planned to last for four years with a possible extension of 4.5 years. The baseline is two long-pointings (LOPs) observing one field for two years apiece. PLATO will collect high-

precision photometric lightcurves of thousands of stars, which will be of particular interest for asteroseismological studies. To reach its objectives, the PLATO mission has defined a core programme with several types of stellar samples. Here, we focus on the P1, P2, and P5 samples. The P1 and P2 samples (hereafter, P1P2) consist in the brightest PLATO targets which will be observed with a 25 s cadence. The P1 sample (resp., P2) includes at least 15 000 (resp., 1000) dwarf and subgiant stars (types F5 to K7), with  $V \leq 11$  mag (resp.  $V \leq 8.5$ ) observed over the mission and a noise level of  $<50$  ppm  $h^{1/2}$ . The noise level of those samples has been adapted to enable precise seismological studies. The P5 sample contains at least 245 000 dwarf and subgiant stars (F5-K7), with  $V \leq 13$  mag cumulative over two target fields. Sampling of these light curves will be 600 s, but it is planned to acquire light curves with a shorter cadence of 50 s for the brightest targets in P5 or for targets of particular interest. For that reason, we also consider the stars of the P5 sample. Input information about the stars in those samples has been gathered in the Input PLATO Catalogue (PIC; Montalto et al. 2021; Nascimbeni et al. 2022). Here, we use version PICv1.0.0. For more details about the PLATO project, we refer to Rauer et al. (2014) and Rauer et al. (in prep.).

Asteroseismology, namely, the detection, measurement, and analysis of stellar oscillations, is one of the main tools that will be used in the framework of the PLATO mission to achieve these objectives. The mission is indeed designed to detect stellar oscillation modes for different classes of stars, including solar-type ones which are its prime targets for exoplanet detection. Asteroseismology can be used to infer the stellar properties, either by measuring global seismic parameters such as  $\nu_{\max}$ , the frequency at which the oscillation modes have their maximum amplitude, and/or  $\Delta\nu$ , the large frequency separation, which characterizes the pattern of power spectra of solar-like oscillations. In ideal conditions, we can precisely measure the frequencies, amplitudes, and widths of individual oscillation modes, which then provide tighter constraints on the stellar mass, radius, and age.

Starting with the Sun, two decades of observations have demonstrated that solar-like oscillations offer a powerful way to derive precise stellar masses, radii, densities, and ages, provided that high-quality seismic parameters are available (see for instance the reviews by [Chaplin & Miglio 2013](#); [Christensen-Dalsgaard 2016, 2018](#); [García & Ballot 2019](#); [Jackiewicz 2021](#); [Serenelli et al. 2021](#)). However, this requires short-cadence (less than 1 mn for dwarfs and subgiants), ultra-high photometric precision (at the level of parts-per-million or ppm), and nearly-uninterrupted long-duration (from months to years) monitoring.

Here, we investigate the seismic performances of the core programme of the PLATO mission; more precisely, our goal is twofold: 1) to obtain an estimate of the number of stars of the PLATO Catalogue for which solar-like oscillations can be detected and 2) to obtain an estimate of the uncertainties on the stellar mass, radius, and age inferences in cases where the data are of high enough quality that individual modes can be detected and their frequencies be measured. By uncertainties here we mean those statistical errors which can only be decreased with higher quality observations (i.e. higher S/N values and longer observation times). We then estimate the (statistical) uncertainties on stellar mass, radius, and age, which result from the propagation of observational errors on the seismic data. We stress that systematic errors and/or biases must be added to the statistical errors to obtain the final error budget. In the present case, systematic errors and/or biases mostly depend on our ability to improve our stellar modelling. This is only briefly discussed at the end of the paper.

The paper is organized as follows. In Sect. 2, we detail the theoretical approach we used to derive the probability of detection of solar-like oscillations. The calculation is based on [Chaplin et al. \(2011b, hereafter C11\)](#)'s methodology which was developed for studying the asteroseismic potential of the *Kepler* mission and later on used for the TESS ([Campante et al. 2016](#); [Schofield et al. 2019](#)) and CHEOPS ([Moya et al. 2018](#)) missions. In order to validate our own computations, we use several samples of stars observed by the NASA *Kepler* mission ([Borucki & Koch 2010](#); [Koch et al. 2010](#)) with and without detected solar-like oscillations. These test samples are presented in Sect. 3, together with the results about the reliability of the detection probability. In Sect. 4, we present our approach to estimate the uncertainties in the seismic inferences of stellar masses, radii, and ages (hereafter, MRA) when assuming that frequencies of individual modes can be measured. In Sect. 5, we present the computations of the detection probabilities for stars in the P1P2 and P5 samples. Those calculations predict the number of stars in each sample for which we expect to detect solar-like oscillations in the core programme of PLATO. As assumed by the PLATO consortium, we consider two observational condi-

tions: 1) we take the adopted noise level arising from observations from nominal 24 cameras at the beginning of life (BOL), so there is no degradation of the instrument; and 2) we take the noise level arising from observations by 22 cameras only at the end of life (EOL), allowing for some degradation of the instrument as usually taken as reference by ESA. We use the noise level given in the PIC that takes into account the fact that each target is observed by either 6, 12, 18, or 24 cameras ([Montalto et al. 2021](#); [Nascimbeni et al. 2022](#)). The calculations are carried out for one LOP which will continuously observe the same field for at least two years. In Sect. 6, for stars in the P1P2 samples with positive seismic detection, we compute the expected uncertainties of the individual frequencies and deduce the resulting MRA uncertainties using the approach described in Sect. 4. A summary and some discussion are provided in Sect. 7. Finally, we give our conclusions in Sect. 8.

## 2. Global solar-like oscillation detection level

### 2.1. Detection probability

In this section, we derive the formalism for computing the detection probability of solar-like oscillations,  $P_{\text{det}}$ , in the photometric power density spectra. It is the probability that such oscillations are detected globally in the power spectrum, not to be confused with the probability to detect and measure the properties of individual oscillation modes.  $P_{\text{det}}$  is calculated according to Eqs. (26) and (28) of [C11](#). The statistics of the power spectrum is a  $\chi^2$  with  $2N_b$  degrees of freedom, where  $N_b$  is the number of independent bins in the envelope band,  $\delta\nu_{\text{env}}$ , of the power spectrum. The probability of having a peak above a given level  $s$ , due to noise only, in the binned power spectrum is then given by Eq. (1) of [Appourchaux \(2004\)](#), namely,

$$P(s' > s, N_b) = \int_s^\infty \frac{1}{\Gamma(N_b)} \frac{u^{N_b-1}}{S^{N_b}} e^{-u/S} du, \quad (1)$$

where  $S$  is the mean of the power spectrum and  $\Gamma(n)$  is the Gamma function.

Here we seek the probability for any value  $s'$  to be larger than a given level  $s$  for a binned power spectrum normalised to the noise level,  $S/N$ ,

$$P(s' > s, N_b) = \int_s^\infty \frac{1}{\Gamma(N_b)} \frac{u^{N_b-1}}{(S/N)^{N_b}} e^{-u/(S/N)} du. \quad (2)$$

With the change of variable  $u' = u/(S/N)$ , the probability is given by

$$P(x' > x, N_b) = \int_x^\infty \frac{1}{\Gamma(N_b)} u'^{N_b-1} e^{-u'} du', \quad (3)$$

which is the probability that the normalised power take any value  $x' = (S/N)'$  larger than a given level  $x = S/N$ . For  $x \rightarrow 0$ , that is  $S \rightarrow 0$ , corresponding to no signal in the power spectrum, the above probability is  $P = 1$  as expected. We note that for convenience, [C11](#) considered a slightly different formulation and calculated the probability that any value  $x' = [(S + N)/N]'$  is larger than a given level  $x = (S + N)/N$ , so that in absence of signal  $S$ ,  $x = 1$ , an approach which we use in the following.

As in [C11](#), using the above equation, we first calculate a signal threshold  $S_{\text{thres}}$  such that the probability for any value  $S \geq S_{\text{thres}}$  to be due to pure noise is smaller than a predefined value  $p_{\text{fa}}$  (false alarm probability). In practice, we remain very conservative and choose a very small value for this false alarm probability,  $p_{\text{fa}} = 0.1\%$ .

In a second step, following C11, we now consider that there is some seismic signal  $S_{\text{mod}}$  in the power spectrum. We obtain the probability of detection of this signal within the false alarm probability  $p_{\text{fa}}$  as the probability of being above the threshold defined previously (Eq. (3)), but with a new normalisation by  $S_{\text{mod}} + N$ ,

$$P_{\text{det}} \equiv P(s' > S_{\text{thres}} + N) = \int_{S_{\text{thres}} + N}^{\infty} \frac{1}{\Gamma(N_b)} \frac{u^{N_b-1}}{(S_{\text{mod}} + N)^{N_b}} e^{-u/(S_{\text{mod}} + N)} du. \quad (4)$$

Choosing as before  $u' = u/(S_{\text{mod}} + N)$  as the new variable, we obtain

$$P_{\text{det}} = \int_{u_0}^{\infty} \frac{1}{\Gamma(N_b)} \frac{[(S_{\text{mod}} + N)u']^{N_b-1}}{(S_{\text{mod}} + N)^{N_b}} e^{-u'} (S_{\text{mod}} + N) du', \quad (5)$$

which finally becomes

$$P_{\text{det}} = \int_{u_0}^{\infty} \frac{1}{\Gamma(N_b)} u'^{N_b-1} e^{-u'} du', \quad (6)$$

where

$$u_0 = \frac{S_{\text{thres}} + N}{S_{\text{mod}} + N} = \frac{1 + (S/N)_{\text{thres}}}{1 + (S/N)_{\text{mod}}}, \quad (7)$$

and  $(S/N)_{\text{thres}}$  is given by the solution of Eq. (3) for  $P = p_{\text{fa}}$ . We note that Eqs. (6) and (7) are equivalent to Eqs. (28) and (29) of C11.

In practice, the probability  $P_{\text{det}}$  can be computed for any particular target of PLATO or any other mission, such as *Kepler*, as soon as we have determined: (i) the signal-to-noise ratio (S/N) in the power spectrum  $(S/N)_{\text{mod}}$  and (ii) the number  $N_b$  of bins to consider in the envelope band of the oscillation modes. The derivation of these two quantities is detailed below. The last technical difficulty is then the computation of the  $\Gamma$  function for the expected very large values of  $N_b$ , which we perform using the classical asymptotic approximation,

$$\ln(\Gamma(n)) \approx (n - 1/2) \ln(n) - n + 1/2 \ln(2\pi),$$

which is valid for large values of  $n$ .

We consider that there is detection of power excess due to solar-like oscillations when the probability  $P_{\text{det}} > 0.99$ . Power spectra showing peaks above  $S_{\text{thres}}$  as defined by Eq. (3) for  $p_{\text{fa}} = 0.1\%$ , but with  $P_{\text{det}} \leq 0.99$  are considered as potentially indicating solar-like oscillations, but with too little confidence to derive any global seismic parameters, let alone properties of individual modes. This is a very conservative position, so that the resulting detection probability can be considered as a lower limit of what can be expected with PLATO.

### 2.1.1. Global S/N in the power spectrum

The global S/N entering Eq. (7) is calculated as

$$(S/N)_{\text{mod}} = \frac{P_{\text{tot}}}{N_{\text{tot}}}, \quad (8)$$

where  $P_{\text{tot}}$  is the total power density in the oscillations and  $N_{\text{tot}}$  the total power density in the noise, both quantities being estimated near  $\nu_{\text{max}}$ , the frequency where the oscillations reach their maximum amplitude. In the following, we detail how these two quantities were calculated.

### 2.1.2. Oscillation power density $P_{\text{tot}}$

The calculation of the oscillation power density  $P_{\text{tot}}$  (in  $\text{ppm}^2/\mu\text{Hz}$ ) can be performed using a formulation as established by C11 restricted to the calculation of the probability of a global detection of power excess due to solar-like oscillations. The power density (in  $\text{ppm}^2/\mu\text{Hz}$ ) is given by (Eq. (19) in C11):

$$P_{\text{tot}} \simeq \frac{1}{2} \frac{V_{\text{mod}}^2 A_{\text{max}}^2}{\Delta\nu}, \quad (9)$$

where  $\Delta\nu$  is in  $\mu\text{Hz}$ ,  $V_{\text{mod}}^2 \simeq 3.1$  is the average visibility calculated for a set of 4 modes  $\ell = 0-3$  (Ballot et al. 2011), and  $A_{\text{max}}$  (in ppm) is the maximum oscillation amplitude of modes, reached at frequency  $\nu \simeq \nu_{\text{max}}$ . The scaling laws for the determination of  $\Delta\nu$  are given in Appendix A. The estimate of  $A_{\text{max}}$  is discussed in Sect. 2.2 and Appendix A.

### 2.1.3. Noise power density $N_{\text{tot}}$

We must also estimate the total noise power density,  $N_{\text{tot}}$ . It is composed on the one hand of the instrumental noise,  $N_{\text{inst}}$ , which includes photon noise and all other instrumental contributors to the noise, and on the other hand of the stellar intrinsic noise,  $N_{\text{gran}}$ , which we assume is dominated by granulation noise at the relevant frequencies. The total noise power density is then given by:

$$N_{\text{tot}} = N_{\text{inst}} + N_{\text{gran}}. \quad (10)$$

Following (Samadi et al. 2019, hereafter S19), the granulation noise power density,  $N_{\text{gran}}$ , is calculated as a scaling power law of  $\nu_{\text{max}}$  (i.e. Eq. (36) in S19), as in Kallinger et al. (2014). The instrumental noise,  $N_{\text{inst}}$ , including photon noise as well as all other sources of noise from the instrument or from the background (satellite jitter, readout noise, digitisation noise, stellar background, zodiacal light, etc.), will be a major contributor to the total noise entering the calculation of the  $(S/N)_{\text{mod}}$  term involved in Eq. (7). It depends on which sample of stars is considered: *Kepler* stars or PLATO targets and will be discussed in Sect. 2.2 below.

### 2.1.4. Number of bins in the oscillation mode envelope

Once  $P_{\text{tot}}$  and  $N_{\text{tot}}$ , and thus  $(S/N)_{\text{mod}}$  are determined, we only need to determine the number of frequency bins  $N_b$  in the oscillation envelope in order to apply Eqs. (3)–(6)–(7). This number is given by

$$N_b = \text{Int} \left[ T_{\text{obs}} \delta\nu_{\text{env}} \times 10^{-6} \right], \quad (11)$$

where  $T_{\text{obs}}$  is the total time interval of the photometric monitoring, in seconds,  $\delta\nu_{\text{env}}$  is the frequency range over which the oscillations are present in the power spectrum, in  $\mu\text{Hz}$ , and  $\text{Int}$  denotes the integer part.

The parameter  $\delta\nu_{\text{env}}$  entering Eq. (11) is essential, because with the observing time, it controls the number of degrees of freedom of the  $\chi^2$  statistics followed by the power spectrum.

## 2.2. Adopted inputs for the calculation of the detection probability $P_{\text{det}}$

In order to compute the global detection probability  $P_{\text{det}}$ , we must provide as input the S/N, namely,  $(S/N)_{\text{mod}}$ , the width of the envelope of the oscillations,  $\delta\nu_{\text{env}}$ , and the observation time,  $T_{\text{obs}}$ , for each target. The S/N, here,  $(S/N)_{\text{mod}}$  in Eq. (8) involves

**Table 1.** Adopted amplitude formulation for  $A_{\max, \text{scal}}$  ( $A_{\max, \text{C11}}$  and  $A_{\max, \text{S19}}$  are obtained using the scaling relations as in C11 and S19, respectively in Appendix. A.

$\nu_{\max}$	$\leq 2500$	$> 2500$
$M \leq 1.15$	$A_{\max, \text{C11}} * 1.31$	$A_{\max, \text{C11}} * 1.19$
$M > 1.15$	$A_{\max, \text{S19}} * 0.95$	$A_{\max, \text{C11}} * 0.95$

**Notes.** As described in Sect. 2.2 and detailed in Appendix A, the proportionality factors are calibrated to the observations inferred by Lund et al. (2017) ( $\nu_{\max}$  in  $\mu\text{Hz}$ , the mass,  $M$ , in solar units).

the power  $P_{\text{tot}}$ . We estimate  $P_{\text{tot}}$  at its maximum namely, at  $\nu_{\max}$  leading  $(S/N)_{\text{mod}}$  at its maximum which we denote hereafter  $(S/N)_{\text{max}}$  for clarity. We then use Eq. (9) assuming the existence of a regular pattern in a power spectrum every  $\Delta\nu$  and not individual modes.

### 2.2.1. Amplitude at maximum power

The amplitude of maximum power,  $A_{\max}$ , involved in  $P_{\text{tot}}$  is obtained in the literature under the form of an empirical relation depending on some combination of the global parameters among stellar mass, stellar radius, effective temperature and/or equivalently the seismic global parameters  $\nu_{\max}$ , and  $\Delta\nu$ . We consider two relations, respectively given by C11 and S19. Both relations are scaled to the solar values. In Appendix A, we show that our adopted recalibrated theoretical values for  $A_{\max}$ ,  $A_{\max, \text{scal}}$  as given in Table 1, are in good agreement with the observed amplitudes at maximum power  $A_{\max, \text{obs}}$ , as derived by Lund et al. (2017; their Table 3) for the *Kepler* Legacy sample. In Table 1, we show how the stellar mass is derived from the scaling relation Eq. (A.8), relating the mass  $M$  to the effective temperature  $T_{\text{eff}}$  and  $\nu_{\max}$ , namely,

$$\frac{M}{M_{\odot}} = \left( \frac{\nu_{\max}}{\nu_{\max, \odot}} \right)^{-0.28} \left( \frac{T_{\text{eff}}}{T_{\text{eff}, \odot}} \right)^{3/2}. \quad (12)$$

For the *Kepler* samples,  $\nu_{\max}$  values are taken from the measurements by Lund et al. (2017). For the PLATO targets, in Sects. 5 and 6, we will take the stellar radii and effective temperatures from PICv1.1.0 to derive  $\nu_{\max}$ . For the solar values, we adopt  $A_{\max, \text{bol}, \odot} = 2.53$  ppm (rms value, see Michel et al. 2009),  $\nu_{\max, \odot} = 3090$   $\mu\text{Hz}$ ,  $\Delta\nu_{\odot} = 135.1$   $\mu\text{Hz}$ , and  $T_{\text{eff}, \odot} = 5777$  K throughout.

### 2.2.2. Instrumental noise

As discussed in Sect. 2.1.3, we need to estimate the instrumental noise,  $N_{\text{inst}}$ , in the power spectrum. The *Kepler* instrumental noise used by C11 is taken from Gilliland et al. (2010), namely,

$$N_{\text{inst}} = 2 N_{\text{rand}}^2 \times 10^{-6} dt, \quad (13)$$

where  $N_{\text{rand}}$ , the total random noise per time interval of the data series (in  $\text{ppm}^2$ ) is given by

$$N_{\text{rand}}^2 = \alpha \left( 1 + 0.1604 \left( \frac{12}{K_p} \right)^5 \times 10^{-0.4 (12 - K_p)} \right), \quad (14)$$

with

$$\alpha = \frac{10^5}{1.28} \times 10^{-0.4 (12 - K_p)}. \quad (15)$$

In the above equations,  $K_p$  is the *Kepler* magnitude of the star,  $dt$  is the cadence of the photometric series, namely,  $dt = 58.85$  s for the *Kepler* short cadence mode. The remaining factor of 2 in Eq. (13) accounts for the choice of a single-sided power spectrum in C11, a convention that we adopt for the remainder of the paper.

For the PLATO calculations in Sects. 5 and 6, we use the noise level,  $N_{\text{inst}}$ , that is available for each target in the PLATO Catalogue, taking into account all instrumental sources of noise according to the most up-to-date understanding of the instrument (Rauer et al., in prep., and Sect. 5).

### 2.2.3. Width of the envelope of the oscillations, $\delta\nu_{\text{env}}$

The parameter  $\delta\nu_{\text{env}}$  can be measured by the width of the assumed Gaussian-like shape envelope of the oscillations in the power spectrum. Several formulations have been suggested for  $\delta\nu_{\text{env}}$  in the literature. They generally take the form of a scaling relation of the type  $\delta\nu_{\text{env}} = a\nu_{\max}^b$ . The coefficients  $a$  and  $b$  are obtained by fitting the *Kepler* data. Their values differ according to whether one considers MS stars of spectral type G, K or hotter stars of spectral type F or subgiants, or red giants (Kim & Chang 2021 and references therein). For instance, Kim & Chang (2021) found slightly different values depending on the formulation assumed for the granulation noise background. We find that these different relationships remain within the upper and lower limits  $\delta\nu_{\text{env}} = \nu_{\max}$  and  $\delta\nu_{\text{env}} = \nu_{\max}/2$ , respectively. Specifically at low  $\nu_{\max}$  (i.e. for more evolved stars), the curves are close to  $\nu_{\max}/2$ , while the curves approach  $\nu_{\max}$  at higher  $\nu_{\max}$  (i.e. for younger stars). In the following, we therefore consider both cases  $\delta\nu_{\text{env}} = \nu_{\max}$  and  $\delta\nu_{\text{env}} = \nu_{\max}/2$ , but keep the conservative case  $\delta\nu_{\text{env}} = \nu_{\max}/2$  for our baseline and estimate the changes in the detection predictions when using  $\delta\nu_{\text{env}} = \nu_{\max}$ .

### 2.2.4. Main sequence versus subgiant stars

For purpose of discussion presented later on in this work, we distinguish the cases of main sequence stars (MS stars) and subgiants. From a stellar evolutionary point of view, the subgiant phase starts when there is not enough hydrogen left at the centre to produce nuclear energy and kinetic pressure to sustain gravity. We use the central hydrogen mass fraction,  $X_c$ , to define a threshold. The MS stars are then defined with  $X_c \geq 10^{-6}$ . According to our stellar models for the range of mass of interest here and the adopted solar chemical composition, the subgiants satisfy

$$\log \left( \frac{L}{L_{\odot}} \right) > 10 (\log T_{\text{eff}} - 3.7532) + 0.25. \quad (16)$$

The transition between MS tars and subgiants is located in a HR diagram in Fig. C.1.

**Mass subsamples.** In the present work, we consider that only MS stars with  $M \leq 1.6 M_{\odot}$  can show solar-like oscillations whereas subgiant being evolved and therefore cooler, can still oscillate with solar-like oscillations while being more massive. We therefore study more carefully the sample of MS stars with seismic masses below  $1.6 M_{\odot}$  while no mass restriction is made for the subgiants. The mass threshold corresponds approximately to the transition between stars with no convective core like the Sun and stars with a convective core in the MS. We also draw a specific attention to the subsample of main-sequence (MS) stars with seismic masses  $M \leq 1.2 M_{\odot}$ . The reason is that the stellar requirements of the PLATO mission are established for a star like the Sun (in mass and age).

### 3. Validation of the calculation of the detection probability with *Kepler* stars

The formalism described in Sect. 2 must be validated before being applied to the stars of the PLATO Input Catalogue. Here we use several samples of stars observed by *Kepler*, in order to verify the performance of this formalism in predicting detectability of solar-like oscillations. In other words, we checked with which confidence level Eqs. (3)–(6)–(7), with the above prescriptions for  $P_{\text{tot}}$ ,  $N_{\text{tot}}$  and  $N_{\text{b}}$ , can predict whether or not solar-like oscillations can be detected. For that purpose, we use two types of *Kepler* stars, those for which such oscillations were or were not detected. The confidence level will be measured in terms of false positive and false negative predicted detections.

#### 3.1. *Kepler* data sets for calibration and validation of theoretical calculations

##### 3.1.1. Sample 1: large sample of stars with solar-like oscillations detected by *Kepler*

The first data set used to construct this sample is a compilation of *Kepler* short cadence stars by (Serenelli et al. 2017, hereafter S17). It includes 415 stars with known detected oscillations, as already reported by C11. Since 2011, these stars were further observed over time intervals ranging from 40 days up to 1055 days. For most of these stars, only the global seismic parameters  $\nu_{\text{max}}$  and  $\Delta\nu$  are available.

A second *Kepler* data set used to construct our sample 1 is an updated compilation by (Mathur et al. 2022, hereafter M22) of the *Kepler* short-cadence stars with detected solar-like oscillations, derived on the basis of samples from C11, Chaplin et al. (2014) and S17. It provides a homogeneous catalog of global seismic parameters for 624 stars.

In order to build a final sample of stars with detected oscillations with all the necessary parameters available, we considered the set of 413 stars common to M22 (updated  $\nu_{\text{max}}$  and  $\Delta\nu$ ) and S17 (observing intervals and grid-based inferred stellar mass and radius). In the following we use the updated  $\nu_{\text{max}}$  and  $\Delta\nu$  from M22. In Appendix B, we look at the impact of choosing the values of  $\nu_{\text{max}}$ ,  $\Delta\nu$ , and  $T_{\text{eff}}$  from S17 instead of M22.

##### 3.1.2. Sample 2: large sample of stars with no oscillations detected by *Kepler*

As a second sample, we consider the list of 990 *Kepler* short-cadence main-sequence solar-like stars for which analyses revealed no detected oscillations, as published by Mathur et al. (2019, hereafter M19). For each star in sample 2, the value of  $\nu_{\text{max}}$  is computed according to

$$\frac{\nu_{\text{max}}}{\nu_{\text{max},\odot}} = \frac{g}{g_{\odot}} \left( \frac{T_{\text{eff}}}{T_{\text{eff},\odot}} \right)^{-1/2}, \quad (17)$$

where the surface gravity  $g = GM/R^2$  and  $T_{\text{eff}}$  are taken from M19<sup>1</sup>. Stellar masses are obtained from the seismic scaling law Eq. (12). This provides  $\delta\nu_{\text{env}}$ . The observation time,  $T_{\text{obs}}$ , is taken from KASOC (*Kepler* Asteroseismic Science Operations Center provides asteroseismological data).

Here again, we focused on stars with masses  $M < 1.6 M_{\odot}$ . The resulting set of 833 stars constitutes our final sample of *Kepler* non-oscillating stars (sample 2).

<sup>1</sup> For the star KIC 4464952, we rather use the LAMOST value  $T_{\text{eff}} = 6161 \pm 214$  K.

##### 3.1.3. *Kepler* Legacy sample

Finally, we need to validate and calibrate the calculation of the oscillation maximum amplitude  $A_{\text{max}}$ , as detailed in Appendix A, as well as Libbrecht (1992)'s relation between individual mode frequencies, linewidths, and S/Ns (see Appendix D). We then used the *Kepler* Legacy sample, which is composed of 66 main-sequence stars with the highest quality of seismic data (Lund et al. 2017) (in the following). For those stars, individual modes are identified. Indeed solar-like oscillation modes can be described by spherical harmonics with spherical degree  $\ell$  and azimuthal order  $m$  for their surface geometry and by the radial order  $n$  labelling the overtones of a given  $\ell, m$  mode. When rotation is not taken into account or cannot be detected seismically, the modes are  $m$ -degenerate and the mode frequencies do not depend on  $m$ . This is the case here, so for each individual mode  $\ell, n$ , the frequency, amplitude and line width are measured with the highest precision. For those stars, the observed values of  $\nu_{\text{max}}$  are taken from L17.

#### 3.2. Results of the validation: Performance of the detection probability approach

Our approach for calculating the probability to globally detect solar-like oscillations was tested against the above *Kepler* samples. Using the formalism described in Sect. 2.1 and the various needed inputs as explained in Sect. 2.2, we assessed on the one hand the fraction of *Kepler* targets with detected oscillations for which we predict no detection (false negatives) and on the other hand the fraction of *Kepler* targets with no detected oscillations for which we predict detection (false positives).

In prevision of the investigation for the PLATO case, we made as our baseline the conservative choices of a positive detection when  $P_{\text{det}} > 0.99$  and  $\delta\nu_{\text{env}} = \nu_{\text{max}}/2$ . As summarized in Table B.5, considering the total population of 1349 *Kepler* stars (MS stars with masses  $M < 1.6 M_{\odot}$  and subgiants of all masses, hereafter  $R_1$  sample) with both predicted false seismic positive (186 stars) and negative (40 stars) detections of oscillations in the baseline conditions leads to an underestimate of the number of real detections (false negative) by  $\sim 3\%$  for the PLATO samples. On the other hand, we can see in Table B.5 that one overestimates the number of real detection (false positive) by 14%. If one considers only MS stars with masses  $M \leq 1.2 M_{\odot}$ , we overestimate the number of real detection by 7%. These tests using *Kepler* results confirm that our approach is valid within the quoted uncertainties and will be used for the PLATO targets in Sect. 5. The detailed results of the calculations of the above results, as well as justifications of the choices made for defining our baseline, are given in Appendix B.

We must stress here that the high percentage (14%) of false positive detection for the  $R_1$  sample is mostly due to subgiant stars with masses larger than  $1.6 M_{\odot}$ . If we consider a subsample of stars including both MS stars and subgiants with masses less than  $1.6 M_{\odot}$ , the percentage of false positive detection of 14% decreases to  $\sim 9\%$ .

False positive detections can be due to actual amplitudes being lower than predicted. Several reasons have been put forward to explain lower-than-expected amplitudes for *Kepler* stars, including significant magnetic activity (Chaplin et al. 2011a; M19) and low metallicity (Samadi et al. 2010; M19). This likely depends on the properties of the stars themselves (mass, luminosity, temperature, rotation, magnetism, etc.). M19 provided the iron-to-hydrogen mass fraction [Fe/H] and the photometric proxy for magnetic activity  $S_{\text{ph}}$  (Garcia et al. 2010;

Mathur 2014; Santos et al. 2023) which measures the amplitude of the spot modulation in the light curves and must be considered as a lower limit of the stellar activity (Salabert et al. 2016, 2017). M19 then found that the probability of non detection of solar-type oscillations is  $\sim 98.7\%$  when  $S_{\text{ph}} > 2000$  ppm (for reference, M19 gave  $S_{\text{ph,min}} = 67.4$  ppm and  $S_{\text{ph,max}} = 314.5$  ppm at the minimum and maximum of activity for the Sun and that the solar oscillation amplitudes decrease by  $12.5\%$  from minimum to maximum of activity). Concerning the impact of metallicity, the magnitude of the amplitude decrease due to a low metallicity remains uncertain and solar-like oscillations have been detected for some metal poor stars. So there is no clear one-to-one correspondence between metallicity and non detection of solar-like oscillation. Nevertheless it is still of interest to look at the 146 stars with false positive detection that have values for  $S_{\text{ph}}$  and  $[\text{Fe}/\text{H}]$  in the M19 sample. This subsample includes 100 subgiants among which 72 with masses larger than  $1.6 M_{\odot}$ . We then note that none of those 72 subgiants have high stellar activity and only 38 of them are metal poor compared to the Sun ( $[\text{Fe}/\text{H}] < -0.1$ ). We also considered the whole sample of 146 stars with false positive detection and available values for  $S_{\text{ph}}$  and  $[\text{Fe}/\text{H}]$  and found 82 stars with a high activity level ( $S_{\text{ph}} > 2000$ ) or  $[\text{Fe}/\text{H}] < -0.1$ . Removing those 82 stars from the original sample of 186 stars with false positive detection leaves 104 stars. Using 104 stars instead of the original 186 stars with false positive detections, we find that the percentage of false positive for the  $R_1$  sample drops to  $\sim 7.7\%$ .

In any case, taking into account stellar activity and metallicity, and/or additional specific properties of the stars to explain the whole sample of false detections would deserve further investigation but is out of scope of the present paper. Since such detailed information are not yet available for the PIC 1.1.0 stars we will therefore keep a conservative value of  $14\%$  for the false positive uncertainty. Accordingly we later give the values of  $X$  together with their uncertainties under the form  $X_{-14\%}^{+3\%}$  for the PLATO subsample of MS stars with masses  $M < 1.6 M_{\odot}$  and subgiants of all masses. However, as an optimist remark, let us stress that stars in the M19 sample were observed over one month only. As the S/N increases over time, we expect to reach smaller amplitudes, everything else equal, with the PLATO mission and therefore a smaller percentage of false positive detection due to too small oscillation amplitudes.

#### 4. Uncertainties on stellar properties in cases of individual frequency measurements

For estimating the seismic MRA inference performances, we go on to consider the case when the mode frequencies can be measured individually. We derived empirical relations giving the mass and radius relative uncertainties as a function of the uncertainty  $\delta\nu_{\ell=1,\text{max}}$  of the  $\ell = 1$  mode closest to  $\nu_{\text{max}}$ , the frequency at maximum power (those modes have the smallest uncertainties). For that purpose, we used the stellar evolution code CESTAM (Morel & Lebreton 2008; Marques et al. 2013) to build a set of stellar models of MS stars with masses of  $M \leq 1.2 M_{\odot}$ , for which we numerically computed the individual frequencies using the ADIPLS code (Christensen-Dalsgaard 2008). The frequency uncertainties are obtained from a rescaling of the frequency uncertainties derived for a ‘degraded Sun’ (Lund et al. 2017). We then used the above frequency set for each synthetic star in the inference code AIMS (Rendle et al. 2019; Lund & Reese 2018) updated for the present purpose by one of the co-authors (D. Reese) in order to infer the MRA

and their statistical uncertainties. It is known that non seismic constraints play only a minor role when the inference includes a large number (e.g. a few dozen) of highly precise individual frequencies. We nevertheless include uncertainties for non-seismic constraints: a generic  $70\text{ K}$  as an uncertainty for the effective temperature and  $0.05$  dex for the metallicity expected from individual spectroscopic study (e.g see the PASTEL catalogue, Soubiran et al. 2022). For Sun-like stars, differential studies with respect to the Sun are even more precise and accurate (Morel et al. 2021). On purpose, we did not introduce any systematic errors, so that we can estimate the seismic performances specifically due to the quality of the data. We then established a correlation between the MRA uncertainties and the frequency uncertainty  $\delta\nu_{\ell=1,\text{max}}$  which was then fitted. We found the following fitted relations:

$$\begin{cases} \delta M/M = 2.083 \delta\nu_{\ell=1,\text{max}} + 0.046 \\ \delta R/R = 0.707 \delta\nu_{\ell=1,\text{max}} + 0.149, \end{cases} \quad (18)$$

where  $\delta\nu_{\ell=1,\text{max}}$  is in  $\mu\text{Hz}$ . All details of these calculations are presented in Appendix C. The MRA relative uncertainties (Eq. (18)) can then be seen as a lower limit of what can be achieved given the observational constraints (which depend on the observing conditions). Realistic uncertainties require to add systematic errors to obtain the final error budget. This is out of scope of the present work (but see the discussion in Sect. 7).

For the PLATO targets, we determine the (theoretical) uncertainties on the individual frequencies using the Libbrecht (1992) formula (Eq. (D.1)),  $\sigma_{\text{Libb}}$ , which depends on the S/N for that particular mode and on the duration of the observation and has proven to yield the right order of magnitude. The S/N in such a case is given by the power per resolved mode – instead of the global power density in the oscillation envelope as before – over the background noise. The power per resolved mode is related to the height of the mode. Accordingly, the power density per resolved mode is derived from (S19) and Lochard (2003) for a single-sided spectrum (see also Appourchaux 2004):

$$P_{\text{mod}} = 2V_1 \frac{A_{\text{max}}^2}{\pi\Gamma_{\text{max}}}, \quad (19)$$

where  $\Gamma_{\text{max}}$  is the mode linewidth at  $\nu \approx \nu_{\text{max}}$ , expressed in  $\mu\text{Hz}$ . For  $\ell = 1$  modes, the square visibility is  $V_1 = 1.5$  (Ballot et al. 2011). The computation of  $A_{\text{max}}$  is described in Appendix A (see in particular Table A.1). Estimates of the mode linewidths are obtained by a fit of measurements in Lund et al. (2017) as a function of effective temperature (see Appendix D, and in particular Table D.1 for details). The Libbrecht (1992) formula predicts the uncertainty for a single, isolated mode peak such as the  $\ell = 0$  modes. For higher  $\ell$  degree modes, one should take into account the fact that they are comprised of multiple components that might not be resolved; and moreover, the exact appearance of the non-radial modes will depend on the angle of inclination presented by the star, currently unknown for the PLATO targets. We therefore rather adopt an empirical approach using real data from the *Kepler* mission: we establish in Appendix D a relation between the theoretical Libbrecht uncertainty of a  $\ell = 1$  mode at  $\nu_{\text{max}}$ ,  $\sigma_{\text{Libb},\ell=1,\text{max}}$ , and the measured frequency uncertainty  $\delta\nu_{\ell=1,\text{max}}$  for the same mode for stars of the *Kepler* Legacy sample. As found in Fig. D.2, the ratio  $\delta\nu_{\ell=1,\text{max}}/\sigma_{\text{Libb},\ell=1,\text{max}}$  tends to decrease with the effective temperature of the star and the decrease is significant over the effective temperature interval found for the PLATO targets. The fit of the ratio  $\delta\nu_{\ell=1,\text{max}}/\sigma_{\text{Libb},\ell=1,\text{max}}$  as a function of effective tem-

perature for the stars of *Kepler* Legacy sample is shown in see Eq. (D.3) and yields

$$\delta v_{\ell=1,\max} = \sigma_{\text{Libb},\ell=1,\max} \left( 4.89 - 4.18 \frac{T_{\text{eff}}}{6000} \right), \quad (20)$$

valid for  $5000 < T_{\text{eff}} \leq 6200$  K. This roughly corresponds to the effective temperature range of the PLATO targets for which we will compute those uncertainties later on. For each PLATO target, we will compute  $\sigma_{\text{Libb},\ell=1,\max}$  then derive  $\delta v_{\ell=1,\max}$  using Eq. (20), before using Eq. (18) for the stellar mass and radius uncertainties.

## 5. Expected solar-like oscillations with PLATO

In this section, we estimate the number of stars for which solar-like oscillations are expected to be detected with the PLATO mission. For this purpose and as already mentioned, we took for each PLATO target star the stellar radius and effective temperature from PICv1.1.0 (Montalto et al. 2021; Nascimbeni et al. 2022). The luminosity is then derived as:

$$\log \left( \frac{L}{L_{\odot}} \right) = 2 \log \left( \frac{R}{R_{\odot}} \right) + 4 \log \left( \frac{T_{\text{eff}}}{T_{\text{eff},\odot}} \right). \quad (21)$$

We consider, on one hand, the P1P2 sample and, on the other, the P5 sample, both for one LOP. We removed the hot stars that appear in the instability strip using the criterion from C11

$$\log T_{\text{eff}} > \log(8907) - 0.093 \log(L/L_{\odot}). \quad (22)$$

This eliminated only a few stars because the criterion on the temperature of the hot side adopted to construct the PIC is much more severe. We also removed the early red giants from the PIC sample, based on their location in a theoretical Hertzsprung-Russell (HR) diagram. These stars are included in a specific scientific validation sub-catalogue of the PIC (Aerts et al. 2023). PLATO performances for such evolved stars were assessed by Miglio et al. (2017). These stars are located at the base of the red giant branch in a HR diagram which we use as an empirical criterion to remove them. We define the criterion in terms of luminosity and effective temperature by computing and plotting a set of evolutionary tracks with different masses and locating the onset of the red giant branch in the HR diagram. This leads us to remove stars when they satisfy:

$$\log T_{\text{eff}} \leq 3.66 + 0.05 \log \frac{L}{L_{\odot}}. \quad (23)$$

After the removal of hot stars and evolved ones, we are left with a set of 7009 stars in our P1P2 sample and 130 140 stars in our P5 sample for one LOP. The stellar mass was derived from the seismic scaling relation Eq. (12) where  $v_{\max}$  is evaluated here according to Eq. (A.10):

$$\frac{v_{\max}}{v_{\max,\odot}} = \left( \frac{R}{R_{\odot}} \right)^{-1.5625} \left( \frac{T_{\text{eff}}}{T_{\text{eff},\odot}} \right)^{0.78}. \quad (24)$$

Appendix A offers more details. The mass is used only to consider various subsamples of stars when analysing the results of the calculations. MS stars with masses larger than  $1.6 M_{\odot}$  are too hot and therefore unlikely to show solar-like oscillations, except perhaps for the stars with high metallicity. In absence of information about metallicity at the present time, hereafter we exclude MS stars with predicted seismic masses  $M > 1.6 M_{\odot}$ .

The detection probability,  $P_{\text{det}}$ , is obtained using Eq. (6) which involves the  $(S/N)_{\text{max}}$  (Eq. (8)), the observing time  $T_{\text{obs}}$

**Table 2.** Numbers of stars in the P1P2 sample in 1 LOP with expected detection of solar-like oscillations after 730 days of observation and assuming  $\delta v_{\text{env}} = v_{\max}/2$ .

Cases	BOL	EOL
All	5858	5553
MS stars	2751	2449
$M < 1.6$	4744	4439
$M < 1.6$ , MS stars	2732	2430
$M \leq 1.2$	1245	1106
$M \leq 1.2$ , MS stars	1016	830
$R \leq 1.1$	269	203

**Notes.** Stellar masses,  $M$ , and radii  $R$  in solar units.

**Table 3.** Number of stars in the P1P2 sample in 1 LOP with expected detection of solar-like oscillations ( $P_{\text{dec}} > 0.99$ ) assuming  $\delta v_{\text{env}} = v_{\max}/2$ .

BOL		
$\delta v_{\text{env}}$	730 days	30 days
$v_{\max}/2$	1245 (5858)	186 (1877)
$v_{\max}$	1541 (6387)	329 (2811)
EOL		
$\delta v_{\text{env}}$	730 days	30 days
$v_{\max}/2$	1106 (5553)	151 (1591)
$v_{\max}$	1389 (6131)	267 (2399)

**Notes.** The numbers without parenthesis correspond to stars with estimated seismic masses  $\leq 1.2 M_{\odot}$ , whereas the numbers in parenthesis correspond to stars with all masses.

and the width of Gaussian-like envelope of the oscillation power spectrum  $\delta v_{\text{env}}$ . The amplitudes,  $A_{\text{max}}$ , used to compute  $(S/N)_{\text{max}}$  are taken according to Table 1. In the calculation of  $N_{\text{tot}}$  (Eq. (10)), we used for  $N_{\text{inst}}$  the PLATO (random and systematic residuals) noise level included in the PIC1.1.0,  $N_{\text{PIC}}$ , for EOL conditions, which was then converted in  $\text{ppm}^2/\mu\text{Hz}$ . For the BOL conditions, we used the data provided by one of the co-authors (Börner et al. 2023). Because the convention in our calculation is a single-sided spectrum as for the power density, we take  $N_{\text{inst}} = 2N_{\text{PIC}}$ . We then added the single-sided stellar granulation background noise as used in S19 (see Sect. 2).

To remain conservative, we kept only those stars for which the probability of the signal be due to noise is 0.1% or less and of those stars we kept only stars for which the probability of the signal being due to solar-like oscillation is larger than 99%.

### 5.1. Expected solar-like oscillations within the PLATO P1P2 sample

The predicted numbers of P1P2 target stars with positive oscillation detection obtained in different mass subsamples are collected in Tables 2 and 3. When we apply the (1 LOP, BOL,  $\delta v_{\text{env}} = v_{\max}/2$ ) conditions after two years of observation, we expect to detect solar-like oscillations for at least 5839 stars (of which 2732 MS stars with  $M \leq 1.6 M_{\odot}$  and 3107 subgiants). Figure 1 show the distributions of those stars with expected detected solar-like oscillations as a function of  $\log T_{\text{eff}}$ , stellar mass and radius. One expects to detect solar-like oscillations in a sub-sample of 1245 stars with  $M/M_{\odot} \leq 1.2$  after two years of observation in BOL conditions (Fig. 2). When restricted to

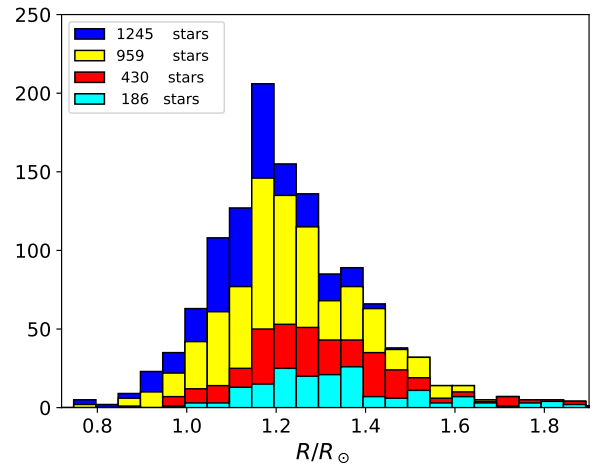
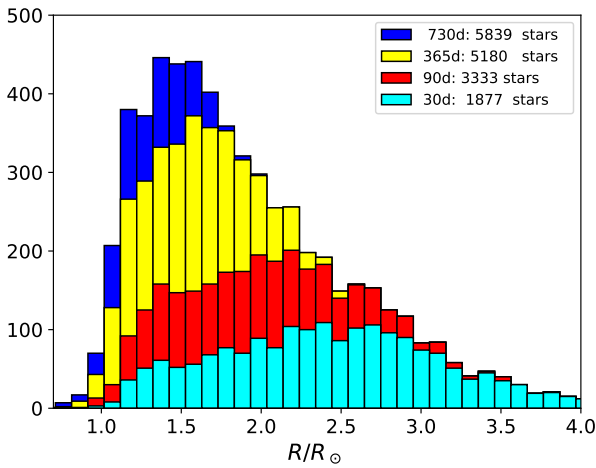
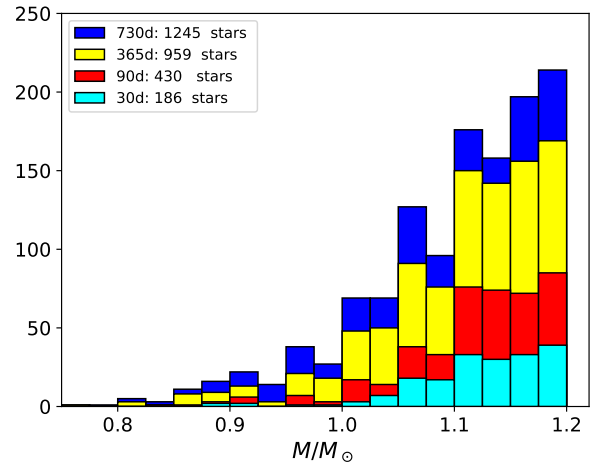
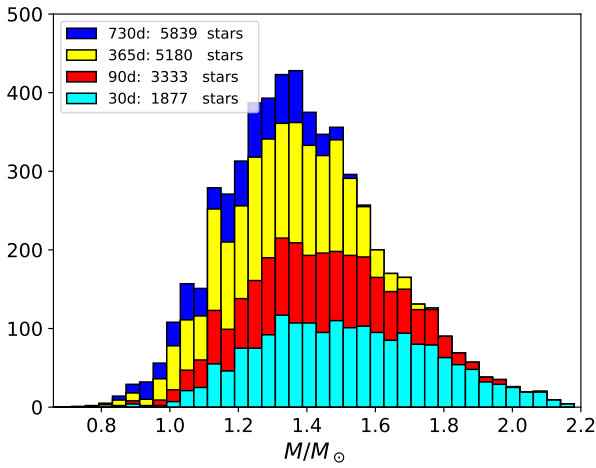
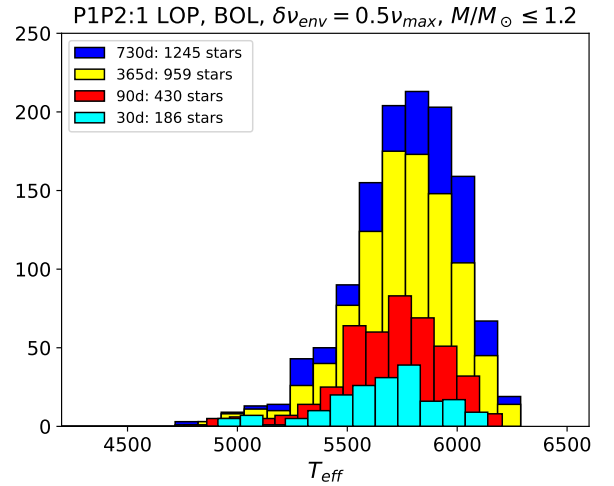
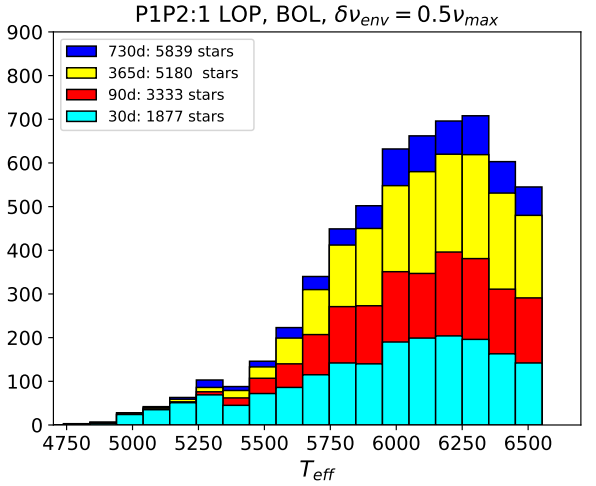


**Fig. 1.** Histograms of the number of stars from the PIP2 sample (subgiants of all masses and MS stars with masses  $M/M_{\odot} < 1.6$ ) with a probability of  $>99\%$  of positive detection of solar-like oscillation in the case of (1 LOP, BOL,  $\delta v_{env} = 0.5v_{max}$ ). Top: distribution in  $T_{eff}$ , middle in stellar mass, bottom in stellar radius. The color code represents the assumed observing duration.

**Fig. 2.** Histograms of the number of stars from the PIP2 sample (with masses  $M/M_{\odot} \leq 1.2$ ) with a probability  $>99\%$  of positive detection of solar-like oscillation in (1 LOP, BOL,  $\delta v_{env} = 0.5v_{max}$ ) conditions. Top: distribution in  $T_{eff}$ ; middle in stellar mass; bottom in stellar radius. The color code represents the assumed observing duration.

MS stars with masses  $\leq 1.2 M_{\odot}$ , the subsample counts 1016 stars. Those stars are small and therefore of the utmost interest for detecting small planets. On the stellar side, more massive stars are likely prone to large systematic uncertainties because

they developed a convective core, the exact extent of which is unknown. Stars with masses  $M \sim 1.2 M_{\odot}$  might also develop a convective core but it is small enough that convective overshoot does not contribute significantly to the total error budget on the age.

**Table 4.** Uncertainties in the number of P1P2 stars with predicted positive seismic detection after 730 days of observations in (1 LOP, BOL) conditions.

$\delta v_{\text{env}}$	$v_{\text{max}}/2$	$v_{\text{max}}$
MS stars ( $M < 1.6$ ) and subgiants	$5839^{+175}_{-818}$	$6997^{+70}_{-1679}$
$M \leq 1.2$	$1245^{+37}_{-87}$	$1541^{+14}_{-170}$

- Impact of BOL/EOL conditions: assuming EOL conditions instead of BOL ones, we would lose a few tens of percent of stars, mostly at small mass and radius (Table 2).
- Impact of  $T_{\text{obs}}$ : as can be expected and be seen in Table 3, the observing time plays an important role. The increase of the number of stars with predicted positive seismic detection is a factor  $\sim 5$ – $7$  greater when increasing the observing time from 30 days to two years. After 30 days, one expects 1877 stars (among which 1596 subgiants), number which increases up to 5858 stars (among which 3107 subgiants) after two years of observation. Not surprisingly, stars for which we might not typically detect solar-like oscillations for too short an observing time are low-mass, MS stars because their oscillation amplitudes are too small. It is also interesting to consider the distributions of stars with positive seismic detection of solar-like oscillations with their magnitudes. Solar oscillations for stars with magnitude  $>10.5$  will be detected only after about one year of observations.
- Impact of uncertainties in the probability calculations: the uncertainties on the number of stars with positive seismic detection due to the uncertainty on  $\delta v_{\text{env}}$  (see Sect.2.5) can be estimated from Table 3. Denoting by  $D$  the number of stars with positive seismic detection, the impact of  $\delta v_{\text{env}}$  uncertainty can be estimated as  $(D_{v_{\text{max}}/2} - D_{v_{\text{max}}})/7009$ , where 7009 is the total number of stars in the initial sample. This yields  $\sim 4\%$  and  $7.5\%$  when considering, respectively the sample of stars with masses  $\leq 1.2 M_{\odot}$  and the sample of all mass stars with positive seismic detection over 730 days in BOL conditions.

We obtain an order of magnitude of the uncertainties on the number of positive detections, say  $X$ , by considering the underestimate due to false negative and the overestimate due to false positive detections. We then used the false negative and positive detection rates derived for our samples 1 and 2 of *Kepler* stars in the option  $\delta v_{\text{env}} = v_{\text{max}}/2$  (second column of Table B.5). This yields  $X^{+3\%}_{-14\%}$  for the sample of MS stars with  $M < 1.6 M_{\odot}$  and subgiants and  $X^{+3\%}_{-7\%}$  for the sample of stars with  $M \leq 1.2 M_{\odot}$  when  $\delta v_{\text{env}} = v_{\text{max}}/2$ . Such uncertainties are provided in Table 4. In percentages, Table 4 indicates a predicted seismic positive detection rate for stars with  $M \leq 1.2 M_{\odot}$  between  $\sim 55$ – $61\%$  (resp.  $65$ – $74\%$ ) of the whole sample of 2099 stars with masses  $\leq 1.2 M_{\odot}$  in BOL conditions after two years of observation taking into account uncertainties due to  $v_{\text{max}}/2$  (resp.  $\delta v_{\text{env}} = v_{\text{max}}$ ). In the same conditions but for the sample of MS stars with masses  $M < 1.6 M_{\odot}$  and subgiants with all masses, the same uncertainties yield predicted seismic positive detections at the level of  $71$ – $86\%$  (resp.  $76$ – $100\%$ ) of the whole sample of 7009 stars in the initial sample taking into account uncertainties due to  $v_{\text{max}}/2$  (resp.  $\delta v_{\text{env}} = v_{\text{max}}$ ).

We note that uncertainties in the probability calculation and the number of stars with expected solar-like oscillation detection can also come from the fact that we used PIC1.1.0 radius and

**Table 5.** Numbers of stars in the P5 sample with expected positive detection ( $P_{\text{det}} > 0.99$ ) of solar-like oscillations in (1 LOP, BOL,  $\delta v_{\text{env}} = 0.5v_{\text{max}}$ ) conditions.

Cases	730d	365d	90d	30d
All	9491	5718	1599	380
MS stars ( $M \leq 1.6 M_{\odot}$ ) & Subgiants of all masses	9486	5716	1599	380
Subgiants of all masses	8877	5657	1599	380
$M \leq 1.2$	878	392	81	21
MS stars	250	43	0	0
subgiants	628	349	81	21

**Notes.** Masses and radii are given in solar units.

effective temperature to compute the global seismic parameters and derive the seismic mass.

## 5.2. Expected solar-like oscillations within PLATO P5 sample

We carried out the same probability calculation as for the P1P2 sample after removing the same types of stars and assuming again a positive detection for  $P_{\text{det}} > 0.99$  (1 LOP, BOL,  $\delta v_{\text{env}} = v_{\text{max}}/2$ ) conditions. We found that the number of expected positive seismic detections amounts to 9 486 for the sample of MS stars with  $M/M_{\odot} < 1.6$  and subgiants after two years of observation (Table 5).

Here again, we observe a drastic increase in positive seismic detections with the observing time. This is illustrated in Fig. 3. This figure shows the distributions in  $T_{\text{eff}}$ , mass, and radius of P5 MS stars with masses  $M < 1.6 M_{\odot}$  and subgiants with all masses with expected positive detections for different observing durations. The number of stars significantly increases when  $T_{\text{obs}}$  increases beyond 1 year, in particular toward stars with smaller radii. The subgiants outnumber significantly the MS stars for the whole sample of stars with  $M < 1.6 M_{\odot}$  (Table 5). As expected, after only 90 days of observation, only 81 stars with masses  $M \leq 1.2 M_{\odot}$  have a seismic positive detection, all subgiants because their amplitudes (roughly  $\propto L/M$ ) are the highest.

Figure 4 compares the distributions of the PLATO noise level,  $N_{\text{PIC}}$ , taken from the PIC1.1.0 between BOL and EOL conditions for stars with expected positive detection of solar-like oscillations in the case of (1 LOP,  $\delta v_{\text{env}} = v_{\text{max}}/2$ ) for 730 days of observation. By construction, following the PLATO ESA requirements, the stars belonging to the P1P2 sample have  $N_{\text{PIC}} \leq 50 \text{ ppm h}^{1/2}$  whereas the stars with higher noise levels constitute the P5 sample. This was based on the EOL conditions. Assuming that the more optimistic BOL conditions hold, we find that 115 MS stars with mass  $M \leq 1.2 M_{\odot}$  in the P5 sample have  $N_{\text{PIC}} \leq 50 \text{ ppm h}^{1/2}$  and could be reclassified as P1 stars, increasing the number of P1P2 stars from 1016 (Table 2) to 1131 that is an increase of the positive detection rate from 15% to above 17%.

## 6. PLATO seismic performances for MRA inferences in the P1P2 sample

For the subset P1P2 stars with expected solar-like oscillations, the detection and highly precise measurement of individual frequencies for a significant number of modes is ensured by the selection of a high S/N by construction. This will allow us to satisfy the requirements that must be achieved by the PLATO mission (PLATO Science Requirements Document

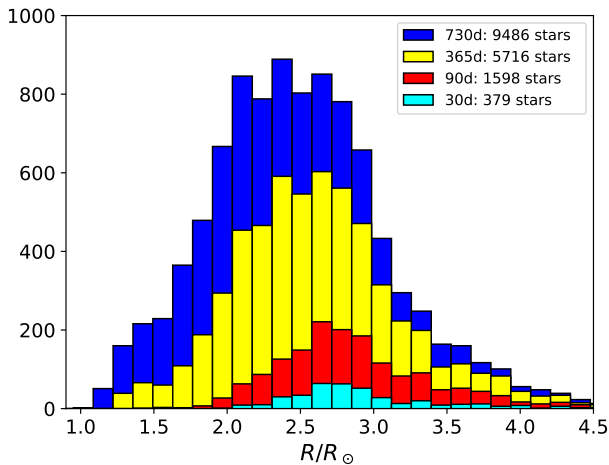
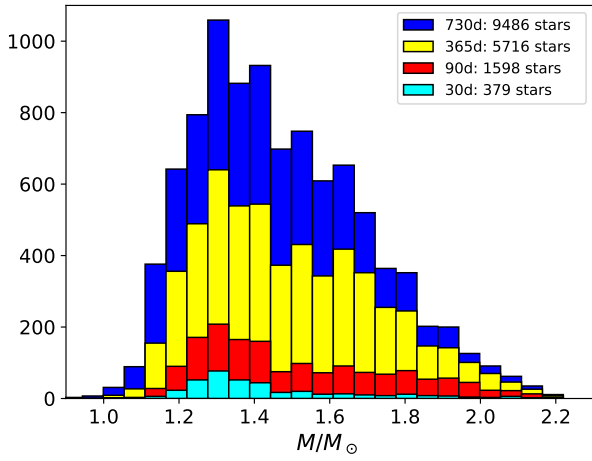
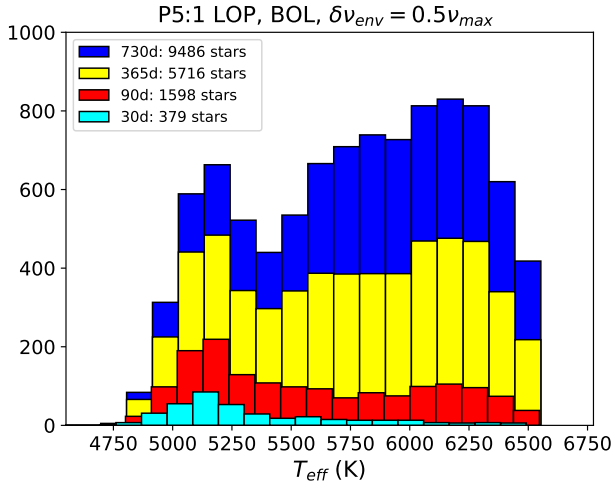


**Fig. 3.** Histograms of the number of stars (MS stars with  $M < 1.6 M_{\odot}$  and subgiants) from the P5 sample with an expected detection of solar-like oscillations with at least 99% probability assuming 730, 365, 90, and 30 days of observations. Conditions are (1 LOP, BOL,  $\delta v_{\text{env}} = 0.5 v_{\text{max}}$ ).

PTO-EST-SCI-RS-0150, ESA document, June 2021) which are: a mass uncertainty better than 15%, a radius uncertainty lower than 2% and an age uncertainty as low as 10% for a star like the Sun or the PLATO reference star defined as  $1 M_{\odot}$ ,  $1 R_{\odot}$ , and  $T_{\text{eff}} = 6000 \text{ K}$ .

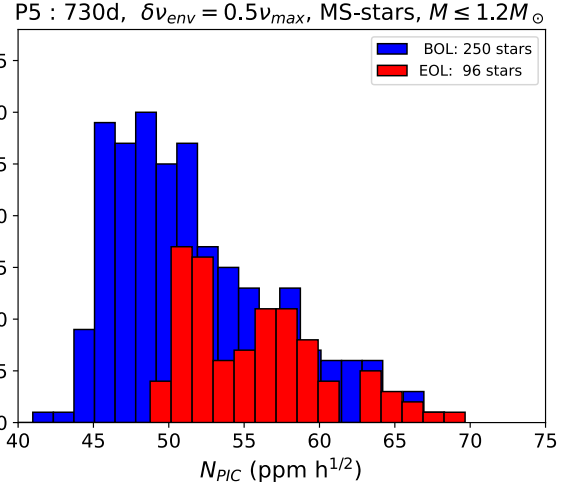


**Fig. 4.** Distributions in  $N_{\text{PIC}}$  (PLATO noise from the PIC1.1.0, in  $\text{ppm h}^{1/2}$ ) of MS stars with  $M \leq 1.2 M_{\odot}$  from the P5 sample with an expected positive detection of solar-like oscillations with a probability higher than 99% assuming 730 days of observations. Conditions are (1 LOP,  $\delta v_{\text{env}} = v_{\text{max}}/2$ ), BOL (blue), EOL (red).

### 6.1. PLATO seismic performances for oscillation frequencies for the P1P2 sample

For the PLATO targets, assuming individual frequencies are available, we can only determine the (theoretical) uncertainty on the frequencies using the Libbrecht (1992) formula (Eq. (D.1)),  $\sigma_{\text{Libb}, \ell=1, \text{max}}$ . We then use Eq. (20) to relate  $\delta v_{\ell=1, \text{max}}$  to  $\sigma_{\ell=1, \text{max}}$  for each target. We computed  $\sigma_{\text{Libb}, \ell=1, \text{max}}$  then  $\delta v_{\ell=1, \text{max}}$  for each target of our P1P2 sample of stars with expected positive seismic detection in BOL condition for 730 days and 90 days. We also included the case where we take into account the scatter in the relation Eq. (20) and the measurement uncertainties in the mode linewidths derived from the *Kepler* stars which leads to multiplying by  $\sqrt{3}$  the Libbrecht's uncertainties  $\sigma_{\text{Libb}, \ell=1, \text{max}}$  (Appendix D). The corresponding distributions of frequency uncertainties  $\delta v_{\ell=1, \text{max}}$  are shown in Fig. 5. In the case (BOL, 730 days,  $\delta v_{\text{env}} = v_{\text{max}}/2$ ) conditions, the bulk of uncertainties are concentrated below  $0.1 \mu\text{Hz}$ . Including the scatter in the relation Eq. (20) shifts up the maxima of the distributions by about  $0.07 \mu\text{Hz}$ . The uncertainties remain below the PLATO requirement of frequency uncertainties  $0.3\text{--}0.5 \mu\text{Hz}$ . In case of 3 months observations, the shift is higher, about  $0.1\text{--}0.13 \mu\text{Hz}$  and the bulk of uncertainties reach  $0.2\text{--}0.3 \mu\text{Hz}$ . When the mode linewidth are increased by a factor  $\sqrt{3}$ , the uncertainties are only slightly shifted with the bulk of uncertainties concentrating around  $0.1 \mu\text{Hz}$ . We also computed the frequency uncertainties in EOL conditions for 730 days but the associated degradation of the signal has only a small impact and is not shown.

### 6.2. PLATO seismic performances for stellar MRA inferences for the P1P2 sample

We now turn to the MRA uncertainties from seismic inferences resulting from the error propagation due to  $\delta v_{\ell=1, \text{max}}$ . We focused on stars with masses  $M \leq 1.2 M_{\odot}$ . We used Eq. (18) to estimate the mass and radius uncertainties as discussed in Sect. 4. We also used the constraint  $\delta v_{\ell=1, \text{max}}$  as a proxy for the constraint on the age uncertainty. The condition  $\delta M/M \leq 3\%$  (often used to obtain an age uncertainty at the level of 10%) can also be added as an additional constraint.

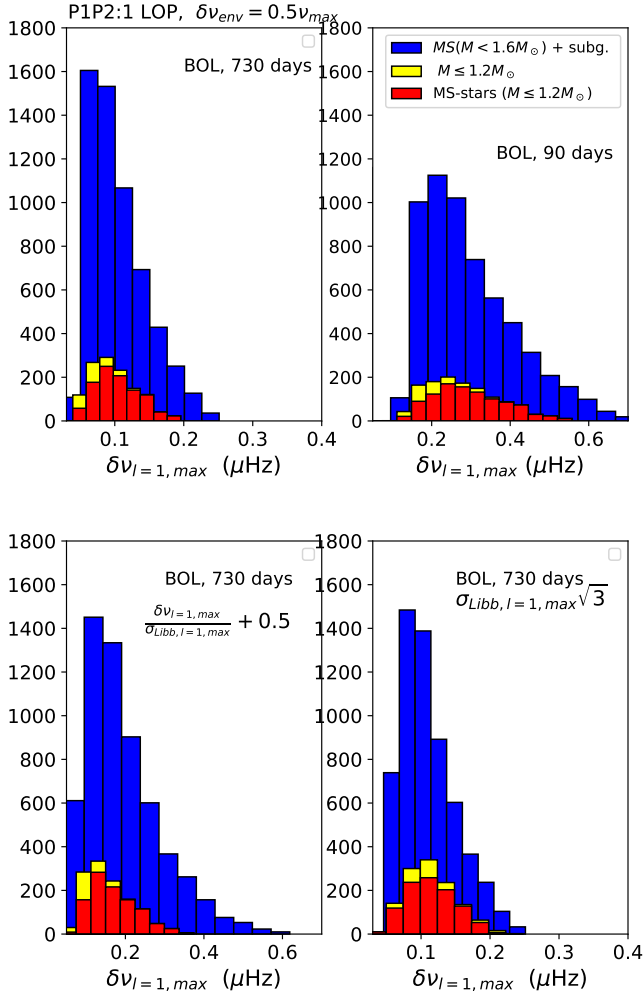


**Fig. 5.** Distribution of frequency uncertainties  $\delta\nu_{\ell=1,\max}$  for the sample of P1P2 stars with expected positive seismic detection. The color code corresponds to different mass samples as indicated in the top right panel. The top panels correspond to the frequency uncertainties computed with Eq. (20) for observation lengths of 730 days (top-left panel) and 90 days (top-right panel). The bottom panels show the frequency uncertainties distribution when one takes into account the scatter in the relation obtained with Eq. (20) (left panel) or the uncertainties in the mode linewidths at low effective temperature width, as per Appendix D (right panel).

We derived the numbers of P1P2 stars with a positive seismic detection while adding successive constraints on the uncertainties giving rise to three cases as follows:

- case I:  $\delta M/M \leq 15\%$  &  $\delta R/R \leq 2\%$ .
- case II:  $\delta M/M \leq 15\%$  &  $\delta R/R \leq 2\%$  &  $\delta\nu_{\ell=1,\max} \leq 0.2 \mu\text{Hz}$ .
- case III:  $\delta M/M \leq 15\%$  &  $\delta R/R \leq 2\%$  &  $\delta\nu_{\ell=1,\max} \leq 0.2 \mu\text{Hz}$  &  $R/R_{\odot} \leq 1.1$ .

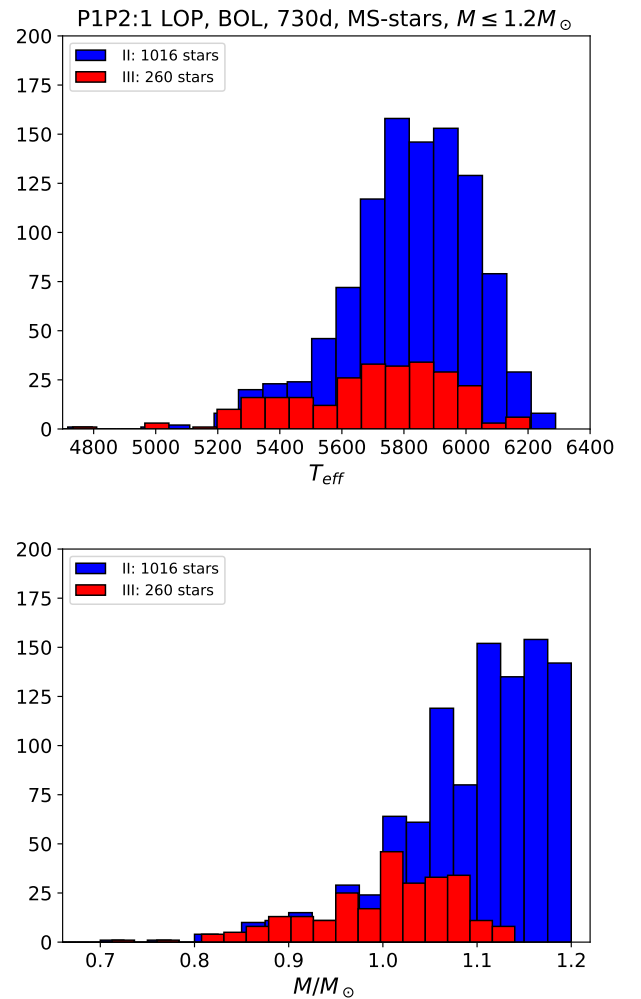
We consider the frequency uncertainties  $\delta\nu_{\ell=1,\max}$  as given by Eq. (20) or Eq. (D.3) without (case a) and with (case b) a +0.5 shift due to the scatter in the fitted relation between  $\delta\nu_{\ell=1,\max}$  and  $\sigma_{\text{Libb},\ell=1,\max}$  (Appendix D). The results are listed in Table 6.

Figure 6 shows the distributions of MS stars with masses  $M \leq 1.2 M_{\odot}$  corresponding to the cases listed in Table 6 as a function of  $T_{\text{eff}}$ , stellar mass and radius (1 LOP, BOL,  $\delta\nu_{\text{env}} = 0.5\nu_{\text{max}}$  730 days) conditions. We expect that the number of stars decrease when adding new constraints. Case I do not reduce the number of stars compared with the initial sample of P1P2 MS

**Table 6.** Number of MS dwarfs with  $M \leq 1.2 M_{\odot}$  stars in the P1P2 sample with expected positive seismic detection and satisfying different cases of MRA uncertainties.

Case	BOL	EOL
Ia	1016	880
IIa	1016	880
IIIa	260	195
Ib	1016	880
IIb	729	599
IIIb	206	146

**Notes.** Assumed conditions are (1 LOP, BOL, 730 days,  $\delta\nu_{\text{env}} = \nu_{\text{max}}/2$ ). Labels a) and b) refer to frequency uncertainties assumed without and with a +0.5 shift due to the scatter in the fitted relation between  $\delta\nu_{\ell=1,\max}$  and  $\sigma_{\text{Libb},\ell=1,\max}$  (Eq. (D.3)).



**Fig. 6.** Histograms in  $T_{\text{eff}}$  (top), and mass (bottom) for MS stars with  $M/M_{\odot} \leq 1.2$  in the P1P2 sample assuming (1 LOP, BOL, 730 days,  $\delta\nu_{\text{env}} = \nu_{\text{max}}/2$ ) conditions with expected detection of solar-like oscillations and satisfying cases IIa and IIIa listed in Table 6.

stars with masses  $M \leq 1.2 M_{\odot}$  with positive seismic detection. This means that the main constraints are the S/Ns imposed by design and the detection probability. The PLATO requirements for the mass, radius and age uncertainties (case II) of P1P2 stars are automatically satisfied in the PIC, provided the oscillations are detected.

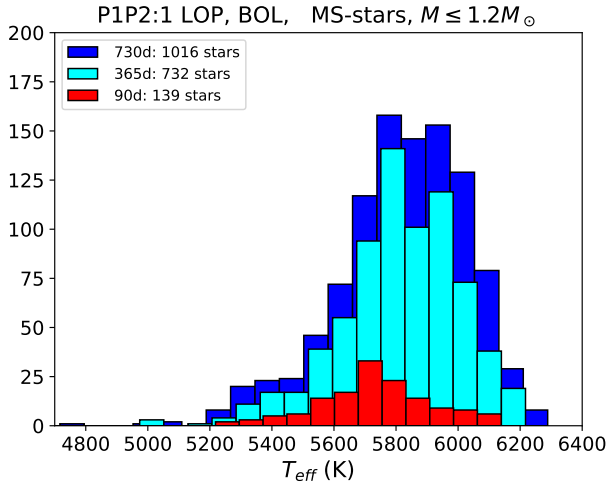


**Fig. 7.** Histogram in  $T_{\text{eff}}$  for the P1P2 subsample of MS stars with  $M/M_{\odot} \leq 1.2$  assuming (1 LOP, BOL,  $\delta v_{\text{env}} = 0.5v_{\text{max}}$ ) conditions and case IIa in Table 6.

Figure 7 shows the histogram of the evolution of the number of these stars when the observation time increases from 90 days to 730 days, assuming (1 LOP, BOL) conditions for MS stars with  $M/M_{\odot} \leq 1.2$ ,  $\delta M/M \leq 15\%$ ;  $\delta R/R \leq 2\%$ , and  $\delta v_{\ell=1,\text{max}} \leq 0.2 \mu\text{Hz}$ . The gain of stars satisfying the PLATO requirements is particularly significant for stars like the reference star when going from 90 days to a year. We note that no such star is found when observing over a short period of time of 30 days.

We also computed the numbers of stars satisfying other constraints such as the case ( $\delta M/M \leq 3\%$ ;  $\delta R/R \leq 2\%$ ); the case ( $\delta v_{\ell=1,\text{max}} \leq 0.5 \mu\text{Hz}$ ) or the case ( $\delta M/M \leq 15\%$ ;  $\delta R/R \leq 2\%$  &  $\delta v_{\ell=1,\text{max}} \leq 0.5 \mu\text{Hz}$ ). The number of stars remains the same as in the initial sample of P1P2 MS stars with masses  $M \leq 1.2 M_{\odot}$  with positive seismic detection.

*Taking into account uncertainties in frequencies and mode linewidths  $\Gamma$  values.* The above numbers of stars remain unchanged when including  $\sim 5\text{-}\sigma$  uncertainties due to scatter in Eq. (18) (Fig. C.4):  $\delta M/M(1 \pm 0.5\%)$ ;  $\delta R/R(1 \pm 0.1\%)$ . In contrast, in the extreme case where one takes into account a scatter of  $+0.5$  in the  $\delta v_{\ell=1,\text{max}}/\sigma_{\text{Libb},\ell=1,\text{max}}$  fitted relation for all stars, the number of MS stars with  $M \leq 1.2 M_{\odot}$  satisfying the PLATO requirement decreases by about 25%.

The impact of degrading the frequency uncertainty  $\delta v_{\ell=1,\text{max}}$  by  $\sqrt{3}$  for stars with  $T_{\text{eff}} \leq 5650 \text{ K}$  (due to uncertainties in the values the mode linewidths, as per Appendix D), instead of the original values of  $\delta v_{\ell=1,\text{max}}$ , leads to a decrease of the number of stars by 38% in case IIb with (BOL, 730d,  $\delta v_{\text{env}} = v_{\text{max}}/2$ ) conditions.

We then conclude that even in the conservative case we considered for the detection probability and in the above worst cases for the frequency uncertainties, the PLATO mission should yield a set of MS stars with a seismic characterisation between  $\sim 80$  and 100 times the *Kepler* Legacy sample assuming two observing fields (i.e. doubling the number of stars obtained for 1 LOP) and depending on whether we assume  $\delta v_{\text{env}} = v_{\text{max}}/2$  or  $v_{\text{max}}$ .

## 7. Summary and discussion

The present study is part of the scientific preparation for the ESA's PLATO mission, which will be launched towards the end of 2026. In this work, we calculate the theoretical probability of

detecting solar-like oscillations for stars belonging to the PLATO Input Catalogue (PIC). More specifically, we considered bright stars (magnitude of 11 and brighter) of the FGK spectral type on the main sequence (masses lower than  $1.6 M_{\odot}$ ) and the subgiant branch. The calculation takes into account the estimated noise level for each individual star, provided by the PIC. Our results indicate that the proportion of stars with positive detections of solar-like oscillations lies within a range of 70%–100% for a continuous observation of two years. The lower (upper) value of this range comes from the assumed narrow (wide) bandwidth of the oscillation spectrum in the Fourier domain for each star, which is the main uncertainty in the calculation. It also depends on the beginning-of-life or end-of-life conditions of the PLATO instrument.

The CoRoT and Kepler missions have taught us that individual oscillation modes can be detected for stars with a noise level of 50 ppm in one hour or less. For the stars in our sample that satisfy this criterion and with positive seismic detection we have estimated the uncertainty in the individual frequency measurements at the maximum of the power spectral density for each star based on the results of the *Kepler* mission. This enabled us to assess the propagation of this statistical error on the seismic inference of the mass, radius, and age of each star. We found that  $\sim 47\text{--}61\%$  of the sample of MS stars with masses  $M \leq 1.2 M_{\odot}$  with statistical uncertainties below the PLATO requirements of 15%, 2% for the stellar masses and radii, respectively and satisfying oscillation frequency uncertainty  $\leq 0.2 \mu\text{Hz}$  at maximum power density amplitude as a proxy for 10% uncertainty of the age of a Sun-like star. Those uncertainties are small enough that they leave margins for including systematic errors while still keeping the total error budget satisfying the PLATO requirements. We note that the masses used to define various mass samples, especially the sample represented by  $M \leq 1.2 M_{\odot}$ , are seismic masses derived from scaling relations. As such, they are approximated as are the number of targets found in each mass subsample but the order of magnitude remains correct.

We also stress that for a few stars, it may be expected that additional errors can come from unexpected issues in the data acquisition or in the variable behavior of the star (such as magnetic activity, Pérez Hernández et al. 2019; Karoff et al. 2019; Thomas et al. 2021; Santos et al. 2023) that can alter the measurements of the frequencies and therefore the MRA uncertainties. From the *Kepler* experience, this could add an uncertainty up to  $0.3 \mu\text{Hz}$  to the statistical uncertainties but it is difficult at this stage to foresee for which stars in the PIC this can happen and this was ignored here.

For the P5 sample, the noise level is higher – again by construction – than for the P1P2 sample in the same (EOL or BOL) conditions. We find a percentage of 7.3–4.3% P5 stars with expected positive seismic detection after 730 days of observation in BOL and EOL conditions, respectively. Among those, a percentage of 0.5–0.2% of P5 MS stars with masses  $M \leq 1.2 M_{\odot}$  are expected to show positive seismic detections. Among them, 115 P5 MS stars with masses  $M \leq 1.2 M_{\odot}$  and with a PIC noise level lower than  $50 \text{ ppm h}^{1/2}$  in BOL conditions satisfy the above PLATO requirements, which means that those stars could be re-classified as P1 stars.

Accordingly, and as a whole, the calculations yield a total of 1131 MS stars with masses  $M \leq 1.2 M_{\odot}$  for which one expects a positive seismic detection and seismic analyses providing mass, radius, and age satisfying the above PLATO requirements in BOL conditions after two years of observation for one LOP. The stars of this sample are plotted in a HR diagram in Fig. 8. For each target, the luminosity is derived with Eq. (21)

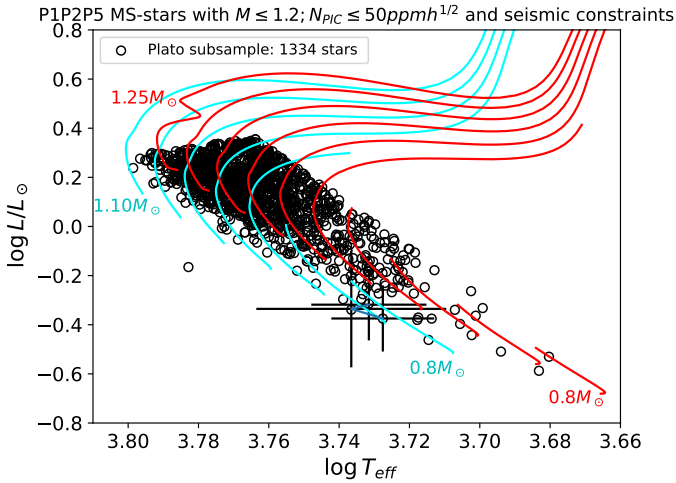


**Fig. 8.** P1, P2, P5 stars with  $M \leq 1.2 M_{\odot}$ ,  $N_{\text{PIC}} \leq 50 \text{ ppm h}^{1/2}$  and satisfying constraint of case II in Table 6. Crosses indicate the (representative) PIC uncertainties for three target stars. Evolutionary tracks of stellar models built with a given initial chemical composition and  $\alpha_{\text{MLT}}$  value are represented by the same color: cyan ( $\alpha_{\text{MLT}} = 1.845$ ,  $Y_0 = 25$ ,  $(Z/X)_0 = 0.0136$ , no atomic diffusion included, masses in the range  $[0.8-1.10] M_{\odot}$  in steps of  $0.05 M_{\odot}$ ) or red ( $\alpha_{\text{MLT}} = 1.642$ ,  $Y_0 = 0.25$ ,  $(Z/X)_0 = 0.0246$ , atomic diffusion included, masses in the range  $[0.8-1.25] M_{\odot}$  in steps of  $0.05 M_{\odot}$ ).

and the stellar radius and the effective temperature, and their uncertainties taken for the PICv1.1.0. Uncertainties are plotted for three stars as representative of the typical PIC uncertainties in the HR locations. Overplotted over the PLATO targets locations, evolutionary tracks of stellar models cover the mass range of  $[0.8-1.2] M_{\odot}$ . The stellar models were built with the CESTAM code (Morel & Lebreton 2008; Marques et al. 2013) assuming the solar relative chemical abundances AGSS09 (Asplund et al. 2009) with different initial values for  $X_0, Y_0, Z_0$  (namely, the mass fractions of hydrogen  $X_0$ , helium  $Y_0$ , and metallicity representing all heavier chemical elements collectively counted as  $Z_0$ ). The convection is described with the classical MLT formulation (Cox & Giuli 1968) involving the mixing length parameter,  $\alpha_{\text{MLT}}$  (a free parameter representing the efficient of convective transport in 1D stellar models). Otherwise, the input physical assumptions are similar to those of the reference model A described in Lebreton & Goupil (2014). The evolutionary tracks in Fig. 8 were computed until an age of 14 Gyr (on purpose greater than the age of the Universe) for the lowest mass stellar models or stopped at an arbitrary phase of the red giant branch for the most massive ones. Hence assuming one single chemical composition and  $\alpha_{\text{MLT}}$  values – usually taken as for the Sun – would clearly not reproduce the whole extended region in the HR occupied by the PLATO targets with the lowest masses. This remains true even taking into account the observational uncertainties in luminosity and effective temperature and the fact that several stars might belong to binary systems.

The anticipated PLATO sample of  $\sim 2793$  well characterized main sequence stars with masses of  $M < 1.6 M_{\odot}$  in one LOP will contribute to the PLATO set of best seismically characterized stars and is roughly 42 times larger than the *Kepler* Legacy sample and will complement the latter in providing tight constraints on stellar modelling. All these results will be reviewed and revised when confronted in 2.5 years from now with the real PLATO data after launch.

In the present work, we have purposefully estimated only the statistical uncertainties on the frequencies and resulting MRA seismic inferences in order to appreciate the added value due to the expected high quality of the PLATO photometric data. The total error budget, however, must include the uncertainties due to the various systematic errors that can be identified but not fully corrected. Of all stellar properties, the stellar age is by far the most challenging to determine accurately. In most cases indeed, stellar ages of single, field stars can only be determined through stellar modelling (Soderblom 2010; Christensen-Dalsgaard & Silva Aguirre 2018); thus, their accuracy strongly depends on the degree of reliability of the available stellar models. Systematic errors are indeed expected to come mostly from insufficiently realistic stellar modelling (e.g. Lebreton & Montalbán 2010; Christensen-Dalsgaard & Silva Aguirre 2018; Lebreton et al. 2014a,b; Salaris & Cassisi 2017; Dupret 2019; Buldgen 2019).

Thanks to the high quality of data acquired by space missions such as CoRoT (Baglin et al. 2009) and *Kepler*, and currently TESS (Ricker et al. 2015), theoretical studies were initiated in order to identify and quantify the impact of the main systematic errors that contribute the most to the error budget. Studies have been carried out as pure theoretical investigations and hare and hounds exercises (e.g. Appourchaux et al. 2006; Lebreton et al. 2014a; Reese et al. 2016; Cunha et al. 2021) or by modelling specific or sets of stars with the best seismic observations such as the small set of CoRoT stars or the larger set of *Kepler* Legacy stars (e.g. Appourchaux et al. 2008; Benomar et al. 2010; Metcalfe et al. 2012; Lebreton & Goupil 2014; Silva Aguirre et al. 2015, 2017; Creevey et al. 2017; Bellinger et al. 2017; Nsamba et al. 2018; Valle et al. 2020; Ong et al. 2021; Farnir et al. 2020; Bétrisey et al. 2022, 2023, among others). At present, due to lack of accuracy, the age uncertainties for solar-like field stars can increase roughly by  $\sim 5-25\%$  depending on poorly modelled physical processes and unknown initial chemical composition and to  $\sim 15-50\%$  for a more massive star with a convective core.

We consider below two illustrative cases: the ‘degraded Sun’ and the two best studied stars of the Legacy sample.

### 7.1. The ‘degraded Sun’

A natural test of the accuracy of seismic modelling and characterisation is to look at the Sun-as-a-star and compare the results of the seismic MRA inferences to the independently known values of the mass, radius, and age of the Sun. This is now done routinely when inferring the MRA for various sets of *Kepler* stars. We therefore carried out several MRA inferences using the data of the so-called ‘degraded Sun’ of Lund et al. (2017). The frequencies of the ‘degraded Sun’ and their uncertainties were built to match the quality of the *Kepler* Legacy sample ( $\delta\nu_{\ell=1,\text{max}} \sim 0.15 \mu\text{Hz}$  with oscillation modes in the range  $\ell = 0, n = 16-27; \ell = 1, n = 15-27; \ell = 2, n = 16-24; \ell = 3, n = 20$ , Lund et al. 2017). Here again we used a grid-based approach (GBM) with the AIMS code. The observational constraints besides the oscillation frequencies and their uncertainties were taken as:  $T_{\text{eff}} = 5777 \pm 77 \text{ K}$ ,  $[\text{Fe}/\text{H}] = 0 \pm 0.1$ ,  $\nu_{\text{max}} = 3090 \pm 3.9 \mu\text{Hz}$ . We compare the results obtained when using two different grids of stellar models. The Cunha et al. (2021, hereafter C21) for which we recall that the stellar models were computed with MESA evolutionary code (Paxton et al. 2018, and references therein) and the frequencies were computed using with the oscillation code ADIPLS (Christensen-Dalsgaard 2008).

**Table 7.** MRA inference for the ‘degraded Sun’ of one standard deviation or 68% credible intervals about the median values.

Grid	$\delta_X$ (%)	$d_{X,rel}$ (%)	$d_{X,norm}$
Mass			
Mo23	0.20	+0.74	3.7
C21	0.21	-2.51	13
Radius			
Mo23	0.07	+0.02	0.32
C21	0.08	-1.03	13
Age			
Mo23	1.37	+ 2.1	0.97
C21	1.53	-11	6.5
Validation luminosity			
Mo23	0.71	5.5	7.8
C21	0.88	5.3	6.35

The second grid of stellar models (hereafter Mo23) was computed by one of the co-authors (namely, N. Moedas, for more details see Moedas et al., in prep.) using also the MESA code and the frequencies were computed using the GYRE oscillation code (Townsend & Teitler 2013). The input physics, values of free parameters and the reference solar relative chemical abundances differ between both grids. This allows to assess the impact of the main uncertainties in modelling solar-like stars. Intended to be applied to real stars unlike C21, Mo23 used a more updated stellar physics (similar to models D1 in Moedas et al. 2022), namely, it included atomic diffusion of chemical elements that helioseismology taught us is crucial for the modelling of solar-like stars. The reference solar abundances are AGSS09 (Asplund et al. 2009) in Mo23 whereas it is GS98 (Grevesse & Sauval 1998) in C21. For sake of simplicity, Mo23 kept the mixing length value of  $\alpha_{MLT}$  fixed to the calibrated solar value whereas C21 let the convection parameter be adjusted in the fitting process. Because here we dealt with real stars, we had to include surface-effect corrections and adopted the Ball & Gizon (2014b)’s correction in the AIMS inferences with both grids.

Following Reese et al. (2016) and C21, in the particular case of the Sun, we can measure the biases (or departure from accuracy) with  $d_{X,rel} \equiv (X_{fit} - X_{true})/X_{true}$  for  $X = M, R, A$ . We wish then to compare these values to the relative statistical uncertainties  $\delta_X \equiv |\delta X|/X_{fit}$  (%) (where  $|\delta X|$  corresponds to one standard deviation) provided by the MRA inferences with the AIMS’ code. Finally it is also informative to estimate how large are the departures from accuracy compared to statistical uncertainties derived from the GBM approach  $d_{X,norm} \equiv |(X_{fit} - X_{true})|/\delta X$  since we will have only access to the last ones in most PLATO stars. The departure between the seismically inferred values for the solar MRA and the known solar values, taken here as  $4.6 \pm 0.4$  Gyr for the solar age (Houdek & Gough 2007) as measured by  $d_{X,rel}$  are given in Table 7 for the two grids. As expected the accuracy is much higher in the case of the Mo23 grid than for the C21 grid mainly because the C21 grid does not included atomic diffusion. These figures are similar to the values derived in other works which all adopt various different input assumptions and which fall in the range ( $\sim 0.3$ – $4\%$ ) for the mass, ( $\sim 0.1$ – $2\%$ ) for the radius, and for the age  $\sim 2$ – $9\%$  when atomic diffusion is included and  $\sim 15$ – $16\%$  when atomic diffusion is not included (e.g. Silva Aguirre et al. 2017; Creevey et al. 2017; Rendle et al.

2019; Jiang & Gizon 2021; Aguirre Børsen-Koch et al. 2022; Metcalfe et al. 2023).

On the other hand, the  $1\sigma$  uncertainties given by the inference calculations as measured by  $\delta_X$  are comparable between the two grids (in the typical range  $0.5$ – $4\%$  and  $3$ – $8\%$  for the mass and age), relatively independently of the accuracy. Accordingly the departures from accuracy as measured in terms of  $\delta X$  uncertainties ( $d_{X,norm}$ , last column of Table 7) significantly differ between the two calculations and between the fitted parameters MRA. In addition in both cases, the inaccuracies of the derived luminosities, which were not included as input constraints amount to  $5\%$  in both cases. As we want to decrease the inaccuracies at the level of or below the statistical uncertainties, this shows that there is room for improvements in the inference process or in the present solar modelling. This also emphasized the importance of building a set of stars with determination of mass and/or radius, and or age (benchmark stars) independently of stellar modelling as is done for the *Gaia* mission (Heiter et al. 2015a,b) and in preparation for the PLATO mission (Maxted & Creevey 2023).

In the case of the ‘degraded Sun’, the net error budget for the age remains close to  $\sim 10\%$  accuracy. One must nevertheless keep in mind that free parameters entering the solar and stellar modelling (namely, the initial helium abundance, convective efficiency parameter,  $\alpha_{MLT}$ ) are calibrated for the Sun so that the solar model reproduces the radius, luminosity at the age of the Sun. On the seismic side, the surface corrections of the frequency are designed for the theoretical frequencies of the stellar models to match the observed ones. Inaccuracy in the solar modelling are then either compensated or minimized by such procedures. This cannot be done for other solar-like stars and one must either attribute arbitrarily the solar values to the free parameters or adjust them during the fitting process for other stars. This can lead to hidden inaccuracies. What can then be and is done is rather studying the sensitivity of the fitted results to changes in the physical description or the values of the free parameters. This is what was carried out for the two brightest ( $V \sim 6$ ) solar-like stars from the *Kepler* Legacy, which we discuss below.

## 7.2. Best studied stars of the Kepler Legacy

The two best studied stars of the Legacy sample, the stars 16 Cyg A (KIC12069424) and B (KIC12069449) belong to a multiple system and show solar-like oscillations (Metcalfe et al. 2012; Lund et al. 2017). They are bright stars for which interferometric radii are available. We can also assume that they were born with the same chemical composition and have the same age. Unlike the Sun, we have no independent measurements of the masses and independent determinations of their ages. On the other hand, the information of a common age and interferometric radii can act as validation of the inferred results and assessment of the accuracy of the MRA inferences. The most recent studies dedicated to 16 Cyg A,B were those of Bazot (2020), Farnir et al. (2020), Nsamba et al. (2022), Buldgen et al. (2022) who provided references to former works. The uncertainties are found of the order of  $4\%$  and  $15\%$  for the masses and ages, respectively. The interferometric radii are well reproduced with uncertainties of  $2\%$ . As an illustration, we carried out seismic inferences for both stars with the two already mentioned grids C21 and Mo23. We inferred the MRA for each *Kepler* star independently using again the Ball & Gizon (2014a) surface-effect correction for the frequencies. The observational constraints are listed in Table 8. The sample of frequencies are those provided

**Table 8.** Observational constraints for the MRA inferences for 16 Cyg A and B.

	16 Cyg A	16 Cyg B
$T_{\text{eff}}^{(a)}$ (K)	5800 (50)	5750.0 (50)
[Fe/H] <sup>(a)</sup> (dex)	0.11 (0.05)	0.08 (0.05)
$\nu_{\text{max}}^{(b)}$ ( $\mu\text{Hz}$ )	2188.5 (4.6)	2561.3 (5.6)
Validation		
$R/R_{\odot}^{(c)}$	1.22 (0.02)	1.12 (0.02)
$L/L_{\odot}^{(d)}$	1.56 (0.05)	1.27 (0.04)

**References.** (a) [Morel et al. \(2021\)](#) (uncertainties increased arbitrarily); (b) [Lund et al. \(2017\)](#); (c) [White et al. \(2013\)](#); (d) [Metcalf et al. 2012](#).

**Table 9.** Results of MRA inferences (%) for 16 Cyg A and B: 68% credible intervals about the median.

	$\delta M/M$	$\delta R/R$	$\delta A/A$
16 Cyg A			
Mo23	0.33	0.12	1.01
C21	0.10	0.03	0.77
16 Cyg B			
Mo23	0.43	0.14	0.85
C21	0.14	0.06	0.95

**Notes.** 16 Cyg A:  $\delta\nu_{\ell=1,\text{max}} = 0.10 \mu\text{Hz}$  (53 modes); 16 Cyg B:  $\delta\nu_{\ell=1,\text{max}} = 0.04 \mu\text{Hz}$  (52 modes).

**Table 10.** Relative differences (%) between the interferometric radius and the corresponding inferred radius  $\Delta R = (R_{\text{int}} - R_X)/R_{\text{int}}$  for each star.

	Mo23	C21
$\Delta R$	1.27–1.24	1.27–1.32
$\Delta A$	0.65–0.78	1.19–1.00

**Notes.** Relative differences between ages of both stars compared to the inference uncertainties  $\Delta A \equiv (|A_{16\text{CygX}} - \langle A_{16\text{Cyg}} \rangle|)/\delta A$  where  $\langle A_{16\text{Cyg}} \rangle$  is the mean of ages of 16 Cyg A and 16 Cyg B.

by [Lund et al. \(2017\)](#). As can be seen in Table 9, the uncertainties derived from the MRA inference processes are small, namely,  $\sim 1\%$  or below in all MRA cases and with both grids. They are smaller for the C21 grid than the Mo23 grid. At that level of relative uncertainties, this is likely due to a difference in the properties of the grids such as the number of adjusted free parameters or to a difference in density of stellar models in the parameter space around the studied stars. This would deserve further investigation but is out of scope in the present study. As for the accuracy, the relative departure of the inferred radius of each star from its respective interferometric radius is slightly above 1% for both grids (Table 10), showing that the radius is well constrained by seismology, rather independently of the physical description of the stellar models in the grids. Table 10 also gives  $\Delta A = (A_X - \langle A \rangle)/\delta A$ , the relative differences between the age of each star and their average age,  $(A_X - \langle A \rangle)$  for  $X = 16\text{CygA}$  and  $16\text{CygB}$  and  $\langle A \rangle = (A_{16\text{CygA}} + A_{16\text{CygB}})/2$  compared to the relative uncertainties of the inferred ages,  $\delta A$ . This shows that the departure from a common age is of the order of the inference uncertainties.

**Table 11.** Sensitivity to different input physics, number and values of free parameters and reference solar chemical composition  $DM \equiv (M_{\text{Mo23}} - M_{\text{C21}})/M_{\text{Mo23}}$ ;  $DR \equiv (R_{\text{Mo23}} - R_{\text{C21}})/R_{\text{Mo23}}$ ;  $DA \equiv (A_{\text{Mo23}} - A_{\text{C21}})/A_{\text{Mo23}}$ .

	16 Cyg A	16 Cyg B
$DM$ (%)	3.26	2.73
$DR$ (%)	1.14	0.97
$DA$ (%)	-13.00	-13.43

Along with the Sun, the 16 Cyg system is often used to test the sensitivity of the inferred results to the use of new/updated inference approaches or new and updated physical processes implemented in stellar modelling (e.g. [Bellinger et al. 2016](#); [Morel et al. 2021](#); [Nsamba et al. 2021](#); [Rendle et al. 2019](#); [Aguirre Børsen-Koch et al. 2022](#); [Ong et al. 2021](#); [Verma et al. 2022](#); [Farnir et al. 2023](#); [Bétrisey et al. 2023](#); [Metcalf et al. 2023](#)). For instance, [Farnir et al. \(2020\)](#) carried out a comprehensive study of the 16 Cyg A,B binary system by estimating the sensitivity of several uncertainties of the MRA inferences—each at a time— in the physical description of both stars. Taking the extremum values about their centroid values of the full set of calculations, the authors found relative differences of  $\pm 3.7\%$  and  $\pm 7\%$  for the mass and age of 16 Cyg A and for Cyg B. The centroid values fall in the same ranges as found by previous authors. However they were not able to find stellar models of both stars with a common age and the same chemical composition while assuming the same physical description. They had to give up either the assumption of the same chemical composition or assume that the stars undergo different efficiency of the atomic diffusion, probably counteracted by additional transport processes yet to be identified. In our illustrative case, we give in Table 11 the relative differences of the median values for the mass, radius, and age of each star resulting from the inferences using the two grids Mo23 and C21. As is well-known and already seen above with the ‘degraded Sun’ discussion, the age is the most affected by differences between the two grids. Here again the main reason is the inclusion or not of atomic diffusion.

This illustrates the lessons we can learn from the study of seismically well characterized stars.

## 8. Conclusion

We estimated the detection probability of solar-like oscillations for the target stars of the ESA project PLATO as provided by the version 1.1.0 of the PLATO Input Catalogue. The targets belong to different samples: stars with the lowest expected noise level constitute the P1P2 sample (main sequence and subgiant FGK stars with magnitude less or equal to 11) and the P5 sample contains similar types of stars but with a higher noise level. A positive detection was assumed whenever the probability that the signal is due to noise is less or equal to 0.1% and the probability of the signal be due to solar like oscillation is larger than 99%. We then found that we can expect positive detections of solar-like oscillations for  $5858_{-879}^{+176}$  stars in the P1P2 sample in one single field after a two-year run of observation assuming the instrument remains nominal over the two years. The given uncertainties are due to false negative and false positive detections as calibrated with *Kepler* data and likely mostly due the fact that we could not take into account the stellar activity or a non solar chemical composition. For the P5 sample, we find a positive detection of  $9491_{-1424}^{+285}$  stars in the same

observing conditions and assuming the same relative uncertainty percentages. As a whole, we can expect more than 15 000 stars with solar-like oscillations to be compared to the *Kepler* solar-like oscillating (main sequence and subgiant stars) sample of 624 stars (M22).

The S/Ns of the targets in the P1P2 sample is (by construction of the sample) high enough that individual mode frequencies can be measured with high precision. For the P1P2 targets for which we predicted a positive seismic detection, we computed the expected frequency uncertainties. We used the error propagation due to those frequency uncertainties to estimate the relative uncertainties that we must expect for the seismically inferred masses, radii, and ages of those targets.

Focusing on main sequence stars with masses of  $\leq 1.2 M_{\odot}$ , we found that about 1131 stars satisfy the PLATO requirements for the uncertainties of the seismically inferred stellar masses, radii, and ages in one single field after a two-year run of observation. Those stars will constitute an enlarged set of well characterized stars, compared to the *Kepler* Legacy sample, which contains 66 stars, out of which about 31 main sequence stars with mass  $\leq 1.2 M_{\odot}$ .

We note that the PLATO mission is expected to operate for four years, with possible extensions over 4.5 more years. This will make possible to more than double the number of detection of solar-like oscillators or to increase significantly the precision of the measurements (of frequencies and then of MRA inferences), depending on whether we observe several fields or remain longer on one field.

We must stress that to the above uncertainties, we must add uncertainties due to systematic errors that mostly arise from imperfect physical description of our stellar models. Those can contribute up to 5–10% to the age uncertainties depending on the type of stars. Ongoing theoretical works are therefore currently addressing the main problems of inaccuracy. Tests and validations of improvements in the physical description of stellar models must use the best seismically characterized stars at our disposal. While the well-characterized stars of the *Kepler* Legacy sample helped us to identify such stellar modelling biases and offering a path to solving them, further advances are currently limited by the small number of stars able to bring tight constraints on the various modelling issues of solar-like oscillating stars. It is therefore one of the key goals of the PLATO mission to collect a sufficiently large number of stars with the highest quality data that can serve as benchmark stars or calibration stars to improve stellar modelling. The expected sample of PLATO solar-like oscillators will provide a much larger diversity of well-characterized stars than that available today. This will result in a larger and denser parameter space in terms of mass, age, chemical composition, and rotation rate. This will then make it possible to reduce the uncertainties in stellar modelling, particularly with regard to the internal transport processes that mainly affect the determination of stellar ages.

*Acknowledgements.* We would like to thank the anonymous referee for his pertinent comments, which helped to improve the manuscript. This work presents results from the European Space Agency (ESA) space mission PLATO. The PLATO payload, the PLATO Ground Segment, and PLATO data processing are joint developments of ESA and the PLATO Mission Consortium (PMC). Funding for the PMC is provided at national levels, in particular by countries participating in the PLATO Multilateral Agreement (Austria, Belgium, Czech Republic, Denmark, France, Germany, Italy, Netherlands, Portugal, Spain, Sweden, Switzerland, Norway, and United Kingdom) and institutions from Brazil. Members of the PLATO Consortium can be found at <https://platomission.com/>. The ESA PLATO mission website is <https://www.cosmos.esa.int/plato>. We thank the teams working for PLATO for all their work. M.C. acknowledges the support of Fundação

para a Ciência e Tecnologia FCT/MCTES, Portugal, through national funds by these grants UIDB/04434/2020, UIDP/04434/2020.FCT, 2022.03993.PTDC (DOI:10.54499/2022.03993.PTDC) and CEECIND/02619/2017. T.M. acknowledges financial support from Belspo for contract PLATO mission development. Funding for the Stellar Astrophysics Centre was provided by The Danish National Research Foundation (Grant DNR106). M.J.G., C.C., R.S., K.B., R.M.O., D.R., Y.L., B.M., and J.B. acknowledge support from the Centre National d'Études Spatiales (CNES). A.S. acknowledges grants PID2019-108709GB-I00 from Ministry of Science and Innovation (MICINN, Spain), Spanish program Unidad de Excelencia María de Maeztu CEX2020-001058-M, 2021-SGR-1526 (Generalitat de Catalunya), and support from ChETEC-INFRA (EU project no. 101008324) and the Plan de Recuperación, Transformación y Resiliencia (PRTR-C17.11) A.M. acknowledges support from the ERC Consolidator Grant funding scheme (project ASTEROCHRONOMETRY, G.A. n. 772293 <http://www.asterochronometry.eu>). S.M. acknowledges support from the Spanish Ministry of Science and Innovation (MICINN) with the Ramón y Cajal fellowship no. RYC-2015-17697, the grant no. PID2019-107061GB-C66, and the grant no. PID2019-107187GB-I00, and through AEI under the Severo Ochoa Centres of Excellence Program 2020–2023 (CEX2019-000920-S).

## References

- Aerts, C., Brown, D., Cabrera, J., et al. 2023, ScienceCalibration Stars Input Catalogue Requirements Justification, PLATO-KUL-PMC-TN-0001
- Aguirre Børsen-Koch, V., Rørsted, J. L., Justesen, A. B., et al. 2022, *MNRAS*, **509**, 4344
- Appourchaux, T. 2004, *A&A*, **428**, 1039
- Appourchaux, T. 2020, PLATO noise background with the NormalCameras: implication for age determination, PLATO-IAS-SCI-AN-001
- Appourchaux, T., Berthomieu, G., Michel, E., et al. 2006, in The CoRoT Mission Pre-Launch Status - Stellar Seismology and Planet Finding, eds. M. Fridlund, A. Baglin, J. Lochard, & L. Conroy, *ESA Spec. Pub.*, **1306**, 429
- Appourchaux, T., Michel, E., Auvergne, M., et al. 2008, *A&A*, **488**, 705
- Appourchaux, T., Benomar, O., Gruberbauer, M., et al. 2012, *A&A*, **537**, A134
- Asplund, M., Grevesse, N., Sauval, A. J., & Scott, P. 2009, *ARA&A*, **47**, 481
- Baglin, A., Auvergne, M., Barge, P., et al. 2009, in *Transiting Planets*, eds. F. Pont, D. Sasselov, & M. J. Holman, 253, 71
- Ball, W. H., & Gizon, L. 2014a, *A&A*, **568**, A123
- Ball, W. H., & Gizon, L. 2014b, *A&A*, **569**, C2
- Ballot, J., Barban, C., & van't Veer-Menneret, C. 2011, *A&A*, **531**, A124
- Bazot, M. 2020, *A&A*, **635**, A26
- Bellinger, E. P., Angelou, G. C., Hekker, S., et al. 2016, *ApJ*, **830**, 31
- Bellinger, E. P., Angelou, G. C., Hekker, S., et al. 2017, *Eur. Phys. J. Web Conf.*, **160**, 05003
- Benomar, O., Baudin, F., Marques, J. P., et al. 2010, *Astron. Nachr.*, **331**, 956
- Bétrisey, J., Pezzotti, C., Buldgen, G., et al. 2022, *A&A*, **659**, A56
- Bétrisey, J., Buldgen, G., Reese, D. R., et al. 2023, *A&A*, **676**, A10
- Börner, A., Papproth, C., Cabrera, P. G., et al. 2023, *Exp. Astron.*, submitted
- Borucki, W. J., & Koch, D. Kepler Science Team 2010, in *AAS/Division for Planetary Sciences Meeting Abstracts #42*, 47.03
- Buldgen, G. 2019, arXiv e-prints [arXiv:1902.10399]
- Buldgen, G., Farnir, M., Eggenberger, P., et al. 2022, *A&A*, **661**, A143
- Campante, T. L., Schofield, M., Kuszelewicz, J. S., et al. 2016, *ApJ*, **830**, 138
- Chaplin, W. J., & Miglio, A. 2013, *ARA&A*, **51**, 353
- Chaplin, W. J., Basu, S., Huber, D., et al. 2014, *ApJS*, **210**, 1
- Chaplin, W. J., Bedding, T. R., Bonanno, A., et al. 2011a, *ApJ*, **732**, L5
- Chaplin, W. J., Kjeldsen, H., Bedding, T. R., et al. 2011b, *ApJ*, **732**, 54
- Christensen-Dalsgaard, J. 2008, *Ap&SS*, **316**, 113
- Christensen-Dalsgaard, J. 2016, arXiv e-prints [arXiv:1602.06838]
- Christensen-Dalsgaard, J. 2018, in *Variability of the Sun and Sun-Like Stars: from Asteroseismology to Space Weather*, eds. J. P. Rozelot, & E. S. Babayev, 125
- Christensen-Dalsgaard, J., & Silva Aguirre, V. 2018, in *Handbook of Exoplanets*, eds. H. J. Deeg, & J. A. Belmonte, 184
- Corsaro, E., Fröhlich, H. E., Bonanno, A., et al. 2013, *MNRAS*, **430**, 2313
- Cox, J. P., & Giuli, R. T. 1968, *Principles of Stellar Structure* (New York: Gordon and Breach)
- Creevey, O. L., Metcalfe, T. S., Schultheis, M., et al. 2017, *A&A*, **601**, A67
- Cunha, M. S., Roxburgh, I. W., Aguirre Børsen-Koch, V., et al. 2021, *MNRAS*, **508**, 5864
- Dupret, M. A. 2019, arXiv e-prints [arXiv:1901.08809]
- Farnir, M., Dupret, M. A., Buldgen, G., et al. 2020, *A&A*, **644**, A37
- Farnir, M., Valentino, A., Dupret, M. A., & Broomhall, A. M. 2023, *MNRAS*, **521**, A131
- García, R. A., & Ballot, J. 2019, *Liv. Rev. Sol. Phys.*, **16**, 4
- García, R. A., Ballot, J., Mathur, S., Salabert, D., & Regulo, C. 2010, arXiv e-prints [arXiv:1012.0494]

- Gilliland, R. L., Jenkins, J. M., Borucki, W. J., et al. 2010, *ApJ*, 713, L160
- Grevesse, N., & Sauval, A. J. 1998, *Space. Sci. Rev.*, 85, 161
- Heiter, U., Jofré, P., Gustafsson, B., et al. 2015a, *A&A*, 582, A49
- Heiter, U., Lind, K., Asplund, M., et al. 2015b, *Phys. Scr.*, 90, 054010
- Hekker, S. 2020, *Front. Astron. Space Sci.*, 7, 3
- Houdek, G., & Gough, D. O. 2007, in *Unsolved Problems in Stellar Physics: A Conference in Honor of Douglas Gough*, eds. R. J. Stanciliffe, G. Houdek, R. G. Martin, & C. A. Tout, *Am. Inst. Phys. Conf. Ser.*, 948, 219
- Huber, D., Bedding, T. R., Stello, D., et al. 2011, *ApJ*, 743, 143
- Huber, D., Zinn, J., Bojesen-Hansen, M., et al. 2017, *ApJ*, 844, 102
- Jackiewicz, J. 2021, *Front. Astron. Space Sci.*, 7, 102
- Jiang, C., & Gizon, L. 2021, *Res. Astron. Astrophys.*, 21, 226
- Kallinger, T., De Ridder, J., Hekker, S., et al. 2014, *A&A*, 570, A41
- Karoff, C., Metcalfe, T. S., Montet, B. T., et al. 2019, *MNRAS*, 485, 5096
- Kim, K.-B., & Chang, H.-Y. 2021, *New A*, 84, 101522a
- Koch, D. G., Borucki, W. J., Basri, G., et al. 2010, *ApJ*, 713, L79
- Lebreton, Y., & Goupil, M. J. 2014, *A&A*, 569, A21
- Lebreton, Y., Goupil, M. J., & Montalbán, J. 2014a, in *EAS Pub. Ser.*, eds. Y. Lebreton, D. Valls-Gabaud, & C. Charbonnel, 65, 99
- Lebreton, Y., Goupil, M. J., & Montalbán, J. 2014b, in *EAS Pub. Ser.*, eds. Y. Lebreton, D. Valls-Gabaud, & C. Charbonnel, 65, 177
- Lebreton, Y., & Montalbán, J. 2010, *Ap&SS*, 328, 29
- Libbrecht, K. G. 1992, *ApJ*, 387, 712
- Lochard, J. 2003, *IAU Joint Discuss.*, 25, E25
- Lund, M. N., & Reese, D. R. 2018, in *Asteroseismology and Exoplanets: Listening to the Stars and Searching for New Worlds*, eds. T. L. Campante, N. C. Santos, & M. J. P. F. G. Monteiro, *Astrophys. Space Sci. Proc.*, 149
- Lund, M. N., Silva Aguirre, V., Davies, G. R., et al. 2017, *ApJ*, 835, 172
- Marques, J. P., Goupil, M. J., Lebreton, Y., et al. 2013, *A&A*, 549, A74
- Mathur, S. 2014, in *SF2A-2014: Proceedings of the Annual meeting of the French Society of Astronomy and Astrophysics*, eds. J. Ballet, F. Martins, F. Bournaud, R. Monier, & C. Reylé, 257
- Mathur, S., García, R. A., Bugnet, L., et al. 2019, *Front. Astron. Space Sci.*, 6, 46
- Mathur, S., García, R. A., Breton, S., et al. 2022, *A&A*, 657, A31
- Maxted, P., & Creevey, O. 2023, [sciencesconf.org:plato-stesci2023:469767](https://sciencesconf.org/plato-stesci2023/469767)
- Metcalfe, T. S., Chaplin, W. J., Appourchaux, T., et al. 2012, *ApJ*, 748, L10
- Metcalfe, T. S., Townsend, R. H. D., & Ball, W. H. 2023, *Res. Notes AAS*, 7, 164
- Michel, E., Samadi, R., Baudin, F., et al. 2009, *A&A*, 495, 979
- Miglio, A., Chiappini, C., Mosser, B., et al. 2017, *Astron. Nachr.*, 338, 644
- Moedas, N., Deal, M., Bossini, D., & Campilho, B. 2022, *A&A*, 666, A43
- Montalto, M., Piotto, G., Marrese, P. M., et al. 2021, *A&A*, 653, A98
- Morel, P., & Lebreton, Y. 2008, *Ap&SS*, 316, 61
- Morel, T., Creevey, O. L., Montalbán, J., Miglio, A., & Willett, E. 2021, *A&A*, 646, A78
- Moya, A., Barceló Forteza, S., Bonfanti, A., et al. 2018, *A&A*, 620, A203
- Nascimbeni, V., Piotto, G., Börner, A., et al. 2022, *A&A*, 658, A31
- Nsamba, B., Campante, T. L., Monteiro, M. J. P. F. G., et al. 2018, *MNRAS*, 477, 5052
- Nsamba, B., Moedas, N., Campante, T. L., et al. 2021, *MNRAS*, 500, 54
- Nsamba, B., Cunha, M. S., Rocha, C. I. S. A., et al. 2022, *MNRAS*, 514, 893
- Ong, J. M. J., Basu, S., & McKeever, J. M. 2021, *ApJ*, 906, 54
- Paxton, B., Schwab, J., Bauer, E. B., et al. 2018, *ApJS*, 234, 34
- Pérez Hernández, F., García, R. A., Mathur, S., Santos, A. R. G., & Régulo, C. 2019, *Front. Astron. Space Sci.*, 6, 41
- Rauer, H., Catala, C., Aerts, C., et al. 2014, *Exp. Astron.*, 38, 249
- Reese, D. R., Chaplin, W. J., Davies, G. R., et al. 2016, *A&A*, 592, A14
- Rendle, B. M., Buldgen, G., Miglio, A., et al. 2019, *MNRAS*, 484, 771
- Ricker, R., Hendricks, S., Perovich, D. K., Helm, V., & Gerdes, R. 2015, *Geophys. Res. Lett.*, 42, 4447
- Salabert, D., García, R. A., Beck, P. G., et al. 2016, *A&A*, 596, A31
- Salabert, D., García, R. A., Jiménez, A., et al. 2017, *A&A*, 608, A87
- Salaris, M., & Cassisi, S. 2017, *Roy. Soc. Open Sci.*, 4, 170192
- Samadi, R., Ludwig, H. G., Belkacem, K., Goupil, M. J., & Dupret, M. A. 2010, *A&A*, 509, A15
- Samadi, R., Deru, A., Reese, D., et al. 2019, *A&A*, 624, A117
- Santos, A. R. G., Mathur, S., García, R. A., et al. 2023, *A&A*, 672, A56
- Schofield, M., Chaplin, W. J., Huber, D., et al. 2019, *ApJS*, 241, 12
- Serenelli, A., Johnson, J., Huber, D., et al. 2017, *ApJS*, 233, 23
- Serenelli, A., Weiss, A., Aerts, C., et al. 2021, *A&A Rev.*, 29, 4
- Silva Aguirre, V., Davies, G. R., Basu, S., et al. 2015, *MNRAS*, 452, 2127
- Silva Aguirre, V., Lund, M. N., Antia, H. M., et al. 2017, *ApJ*, 835, 173
- Soderblom, D. R. 2010, *ARA&A*, 48, 581
- Soubiran, C., Brouillet, N., & Casamiquela, L. 2022, *VizieR Online Data Catalog: J/A+A/663/A4*
- Stello, D., Chaplin, W. J., Basu, S., Elsworth, Y., & Bedding, T. R. 2009, *MNRAS*, 400, L80
- Thomas, A. E. L., Chaplin, W. J., Basu, S., et al. 2021, *MNRAS*, 502, 5808
- Townsend, R. H. D., & Teitler, S. A. 2013, *MNRAS*, 435, 3406
- Valle, G., Dell’Omodarme, M., Prada Moroni, P. G., & Degl’Innocenti, S. 2020, *A&A*, 635, A77
- Verma, K., Rørsted, J. L., Serenelli, A. M., et al. 2022, *MNRAS*, 515, 1492
- White, T. R., Huber, D., Maestro, V., et al. 2013, *MNRAS*, 433, 1262

- 
- <sup>1</sup> LESIA, Observatoire de Paris, Université PSL, CNRS, Sorbonne Université, Université Paris Cité, 5 place Jules Janssen, 92195 Meudon, France  
e-mail: mariejo.goupil@obspm.fr
  - <sup>2</sup> Institut d’Astrophysique Spatiale, UMR 8617, Université Paris-Saclay, Bâtiment 121, 91045 Orsay, France
  - <sup>3</sup> Instituto de Astrofísica de Canarias (IAC), 38205 La Laguna, Tenerife, Spain
  - <sup>4</sup> Universidad de La Laguna (ULL), Departamento de Astrofísica, 38206 La Laguna, Tenerife, Spain
  - <sup>5</sup> Deutsches Zentrum für Luft- und Raumfahrt e.V. (DLR), Institut für Planetenforschung, Rutherfordstr. 2, 12489 Berlin, Germany
  - <sup>6</sup> Deutsches Zentrum für Luft- und Raumfahrt e.V. (DLR), Institut für Optische Sensorsysteme, Rutherfordstr. 2, 12489 Berlin, Germany
  - <sup>7</sup> Instituto de Astrofísica e Ciências do Espaço, Universidade do Porto, CAUP, Rua das Estrelas, 4150-762 Porto, Portugal
  - <sup>8</sup> Departamento de Física e Astronomia, Faculdade de Ciências da Universidade do Porto, Rua do Campo Alegre, s/n, 4169-007 Porto, Portugal
  - <sup>9</sup> Department of Physics, Indian Institute of Technology (BHU), Varanasi 221005, India
  - <sup>10</sup> Université de Rennes, CNRS, IPR (Institut de Physique de Rennes), UMR 6251, 35000 Rennes, France
  - <sup>11</sup> LUPM, Université de Montpellier, CNRS, Place Eugène Bataillon, 34095 Montpellier, France
  - <sup>12</sup> IRAP, Université de Toulouse, CNRS, CNES, UPS, 14 avenue Édouard Belin, 31400 Toulouse, France
  - <sup>13</sup> School of Physics & Astronomy, University of Birmingham, Edgbaston, Birmingham B15 2TT, UK
  - <sup>14</sup> Stellar Astrophysics Centre, Department of Physics and Astronomy, Aarhus University, Ny Munkegade 120, 8000 Aarhus C, Denmark
  - <sup>15</sup> INAF – Osservatorio Astrofisico di Catania, Via S. Sofia, 78, 95123 Catania, Italy
  - <sup>16</sup> Dipartimento di Fisica e Astronomia, Università degli Studi di Bologna, Via Gobetti 93/2, 40129 Bologna, Italy
  - <sup>17</sup> INAF – Osservatorio di Astrofisica e Scienza dello Spazio di Bologna, Via Gobetti 93/3, 40129 Bologna, Italy
  - <sup>18</sup> Space sciences, Technologies and Astrophysics Research (STAR) Institute, Université de Liège, Quartier Agora, Allée du 6 Août 19c, Bât. B5c, B4000 Liège, Belgium
  - <sup>19</sup> Institute of Space Sciences (ICE, CSIC), Carrer de Can Magrans S/N, 08193 Bellaterra, Spain
  - <sup>20</sup> Institut d’Estudis Espacials de Catalunya (IEEC), Carrer Gran Capita 4, 08034 Barcelona, Spain
  - <sup>21</sup> Université Côte d’Azur, Observatoire de la Côte d’Azur, CNRS, Laboratoire Lagrange, Bd de l’Observatoire, CS 34229, 06304 Nice Cedex 4, France
  - <sup>22</sup> Departament d’Astronomia i Astrofísica, Universitat de València, C. Dr. Moliner 50, 46100 Burjassot, Spain
  - <sup>23</sup> AIM, CEA, CNRS, Univ. Paris-Saclay, Univ. Paris Diderot, Sorbonne Paris Cité, 91191 Gif-sur-Yvette, France

## Appendix A: Validation of adopted input for our theoretical calculations

We determine and validate our theoretical relations and calculations by comparing them with the appropriate *Kepler* data sets described in Sect. 3.1. The goal is to choose the proper recipes for the input parameters that enter the calculation of either the detection probability or the MRA uncertainties for the PLATO target stars.

### A.1. Global seismic parameters and validation of the scaling relation for the seismic mass

The scaling properties of the global seismic parameters are discussed in Chaplin & Miglio (2013), Hekker (2020) and references therein;  $\Delta\nu \propto \bar{\rho}^{1/2} \propto (M/R^3)^{1/2}$  and  $\nu_{\max} \propto g/T_{\text{eff}}^{1/2}$  where  $\bar{\rho}$  and  $g$  are the mean density and the gravity, respectively. When scaled with the solar values, this gives

$$\frac{\nu_{\max}}{\nu_{\max,\odot}} = \left(\frac{M}{M_{\odot}}\right) \left(\frac{R}{R_{\odot}}\right)^{-2} \left(\frac{T_{\text{eff}}}{T_{\text{eff},\odot}}\right)^{-1/2} \quad (\text{A.1})$$

$$\frac{\Delta\nu}{\Delta\nu_{\odot}} = \left(\frac{M}{M_{\odot}}\right)^{1/2} \left(\frac{R}{R_{\odot}}\right)^{-3/2}. \quad (\text{A.2})$$

For the solar values, we adopt  $A_{\text{max,bol},\odot} = 2.53$  ppm (rms value, see Michel et al. 2009),  $\nu_{\max,\odot} = 3090\mu\text{Hz}$ ,  $\Delta\nu_{\odot} = 135.1\mu\text{Hz}$ , and  $T_{\text{eff},\odot} = 5777$  K.

These relations can be inverted to provide the seismic mass and radius provided that  $\nu_{\max}$ ,  $\Delta\nu$ , and  $T_{\text{eff}}$  are known. The inverted relationships read as follows:

$$\frac{M}{M_{\odot}} = \left(\frac{\nu_{\max}}{\nu_{\max,\odot}}\right)^3 \left(\frac{\Delta\nu}{\Delta\nu_{\odot}}\right)^{-4} \left(\frac{T_{\text{eff}}}{T_{\text{eff},\odot}}\right)^{3/2} \quad (\text{A.3})$$

$$\frac{R}{R_{\odot}} = \left(\frac{\nu_{\max}}{\nu_{\max,\odot}}\right) \left(\frac{\Delta\nu}{\Delta\nu_{\odot}}\right)^{-2} \left(\frac{T_{\text{eff}}}{T_{\text{eff},\odot}}\right)^{1/2}. \quad (\text{A.4})$$

Further, it is also well accepted that  $\Delta\nu$  and  $\nu_{\max}$  are tightly correlated (Stello et al. 2009; Huber et al. 2011; Serenelli et al. 2017). Indeed a fit to the *Kepler* data yields

$$\frac{\Delta\nu}{\Delta\nu_{\odot}} = a \left(\frac{\nu_{\max}}{\nu_{\max,\odot}}\right)^s. \quad (\text{A.5})$$

We then use this scaling relation between  $\nu_{\max}$  and  $\Delta\nu$  into Eq. (A.1) above and inverting the resulting equations yields the seismic mass as

$$\frac{M}{M_{\odot}} = a^{-4} \left(\frac{\nu_{\max}}{\nu_{\max,\odot}}\right)^{3-4s} \left(\frac{T_{\text{eff}}}{T_{\text{eff},\odot}}\right)^{3/2}. \quad (\text{A.6})$$

Similarly, the seismic radius is obtained as

$$\frac{R}{R_{\odot}} = a^{-2} \left(\frac{\nu_{\max}}{\nu_{\max,\odot}}\right)^{1-2s} \left(\frac{T_{\text{eff}}}{T_{\text{eff},\odot}}\right)^{1/2}. \quad (\text{A.7})$$

For consistency, we rederived the relation Eq.(A.5) by fitting our *Kepler* data set of solar-like oscillating stars. Figure A.1 shows the variation of  $\Delta\nu$  as a function of  $\nu_{\max}$  for the short cadence *Kepler* data on one hand from the Legacy sample from Lund et al. (2017) (L17) and on the other hand from the S17 catalogue (their Table 3). A fit of the S17's data gives  $a = 0.992$  and  $s = 0.805$  (assuming  $\Delta\nu_{\odot} = 135\mu\text{Hz}$  and  $\nu_{\max,\odot} = 3090\mu\text{Hz}$ )

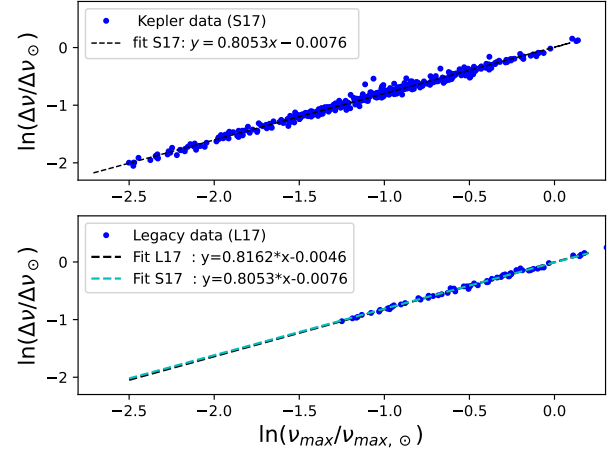


**Fig. A.1.** Scaled  $\Delta\nu$  as a function of scaled  $\nu_{\max}$  in logarithmic scales with  $\Delta\nu_{\odot} = 135\mu\text{Hz}$  and  $\nu_{\max} = 3090\mu\text{Hz}$ . Blue dots: *Kepler* short cadence data. Top: S17's catalogue (S17's table 3). Bottom: Legacy data (L17). Dashed lines are linear fits.

while a fit to L17's data gives  $a = 0.995$  and  $s = 0.816$ , both in satisfactory agreement with relations found in the literature.

We then adopt  $s = 0.82$  and  $a = 1$  in the rest of the paper. We then obtain, from Eq. (A.6), the scaling for the seismic mass as:

$$\frac{M}{M_{\odot}} = \left(\frac{\nu_{\max}}{\nu_{\max,\odot}}\right)^{-0.28} \left(\frac{T_{\text{eff}}}{T_{\text{eff},\odot}}\right)^{3/2}. \quad (\text{A.8})$$

For the radius, we obtain, from Eq. (A.7):

$$\frac{R}{R_{\odot}} = \left(\frac{\nu_{\max}}{\nu_{\max,\odot}}\right)^{-0.64} \left(\frac{T_{\text{eff}}}{T_{\text{eff},\odot}}\right)^{1/2}. \quad (\text{A.9})$$

It is known that the global seismic scaling relations Eqs. (A.1) and Eqs. (A.2) are accurate at the level of a few percents (Huber et al. (2017), S17 and references therein). This is enough for our purpose since masses and radii are only used here to delimitate some sub-samples of stars of interest.

When  $\nu_{\max}$  is not known, it is derived by inverting Eq. (A.9)

$$\frac{\nu_{\max}}{\nu_{\max,\odot}} = \left(\frac{R}{R_{\odot}}\right)^{-1.5625} \left(\frac{T_{\text{eff}}}{T_{\text{eff},\odot}}\right)^{0.78} \quad (\text{A.10})$$

$$\frac{\Delta\nu}{\Delta\nu_{\odot}} = \left(\frac{\nu_{\max}}{\nu_{\max,\odot}}\right)^{0.82} \quad (\text{A.11})$$

The seismic parameter  $\nu_{\max}$  can be obtained from a seismic analysis (e.g. from *Kepler* data) and  $T_{\text{eff}}$  is obtained from a spectroscopic study. Because for the PLATO targets,  $\nu_{\max}$  are not yet known, we use the stellar radius and  $T_{\text{eff}}$  from the PIC to derive  $\nu_{\max}$ .

### A.2. Oscillation power amplitude $A_{\text{max}}$

Both formulations, Eqs. (9) and (19), for the power,  $P_{\text{tot}}$ , involve the oscillation maximum amplitude  $A_{\text{max}}$ . In order to adopt a theoretical relation for the amplitudes, we compare the amplitudes given by two semi-empirical relations derived in C11 and S19 with the measured amplitudes,  $A_{\text{max,obs}}$ , of the *Kepler* Legacy sample by Lund et al. (2017) (their Table 3). We recall that this sample is composed of 66 main-sequence stars with the highest quality of seismic data, and for which individual oscillation

**Table A.1.** Adopted amplitude formulation for  $A_{\max, \text{scal}}$ . Masses,  $M$ , in solar units and  $\nu_{\max}$  in  $\mu\text{Hz}$ .

$\nu_{\max}$	$\leq 2500$	$> 2500$
$M \leq 1.15$	$A_{\max, \text{C11}} * 1.31$	$A_{\max, \text{C11}} * 1.19$
$M > 1.15$	$A_{\max, \text{S19}} * 0.95$	$A_{\max, \text{C11}} * 0.95$

modes are identified and their frequencies, amplitudes, and line widths are measured with the highest level of precision.

On the theoretical side, C11 derived the relation (Eq. 9 in C11):

$$\frac{A_{\max}}{A_{\max, \text{bol}, \odot}} = \beta_{is} \left( \frac{R}{R_{\odot}} \right)^2 \left( \frac{T_{\text{eff}}}{T_{\text{eff}, \odot}} \right)^{1/2}, \quad (\text{A.12})$$

where

$$\beta_{is} = 1 - e^{(T_{\text{eff}} - T_{\text{red}})/1550\text{K}} \quad (\text{A.13})$$

and

$$T_{\text{red}}(\text{K}) = 8907 \left( \frac{L}{L_{\odot}} \right)^{-0.093}, \quad (\text{A.14})$$

$$\frac{L}{L_{\odot}} = \left( \frac{R}{R_{\odot}} \right)^2 \left( \frac{T_{\text{eff}}}{T_{\text{eff}, \odot}} \right)^4. \quad (\text{A.15})$$

S19 used the relation between  $A_{\max}$ ,  $\nu_{\max}$ ,  $\Delta\nu_{\odot}$ , and  $T_{\text{eff}}$  established by Corsaro et al. (2013) based on their model 4 $\beta$  (Eq. 19, Table 3 in Corsaro et al. (2013))

$$\frac{A_{\max}}{A_{\max, \text{bol}, \odot}} = 1.41 \left( \frac{\nu_{\max}}{\nu_{\max, \odot}} \right)^{-2.314} \left( \frac{\Delta\nu}{\Delta\nu_{\odot}} \right)^{2.088} \left( \frac{T_{\text{eff}}}{T_{\text{eff}, \odot}} \right)^{-2.235}, \quad (\text{A.16})$$

valid for  $4000\mu\text{Hz} > \nu_{\max} > 150\mu\text{Hz}$ . We eliminate  $\Delta\nu/\Delta\nu_{\odot}$  with Eq. (A.5). With  $s = 0.82$ ,  $a = 1$ , this yields the second relation that we will consider (S19):

$$\frac{A_{\max}}{A_{\max, \text{bol}, \odot}} = 1.41 \left( \frac{\nu_{\max}}{\nu_{\max, \odot}} \right)^{-0.610} \left( \frac{T_{\text{eff}}}{T_{\text{eff}, \odot}} \right)^{-2.235}. \quad (\text{A.17})$$

Both relations involve the effective temperature  $T_{\text{eff}}$ , C11 also involves the stellar radius and S19 involves  $\nu_{\max}$ . We also need the stellar mass to discriminate between low and high mass cases. The stellar radius and the stellar mass are given by the scaling relation Eq. (A.8).

Figure A.2 compares the amplitudes  $A_{\max, \text{scal}}$  as given in Table A.1 to the observed amplitudes  $A_{\max, \text{obs}}$  for the Legacy sample. The comparison leads us to adopt as best estimate the purely empirical amplitude relations as given in Table A.1. As can be seen in this figure, our empirical calibration of  $A_{\max}$  is quite satisfactory. The rescaling factors 1.19 and 1.31 in Table A.1 can be explained as arising from uncertainties in the estimate of the *Kepler* noise. The threshold  $M = 1.15M_{\odot}$  is arbitrary but reflects the fact that the scatter in  $A_{\max}$  is larger for stars in the high mass regime corresponding to higher effective temperature for which measurements of frequencies, linewidths, and amplitudes are more difficult (Appourchaux et al. 2012). On the theoretical side, the  $1.15M_{\odot}$  threshold corresponds to the discrimination between main sequence stars with and without a convective core.

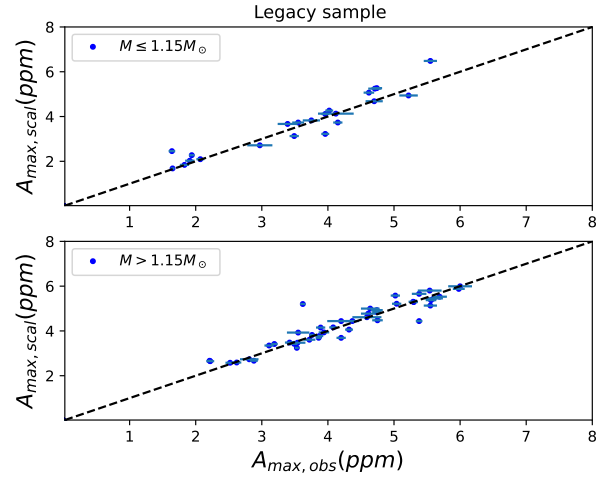


**Fig. A.2.** Comparison of the amplitudes  $A_{\max, \text{scal}}$  computed as given in Table A.1 with the observed amplitudes  $A_{\max, \text{obs}}$  for the LEGACY sample from (Lund et al. 2017).

## Appendix B: Validation for the probability of detection

In order to validate our calculations, we computed the detection probability for the samples of *Kepler* stars with known detection (sample 1) on one hand and the sample of stars for which no solar-like oscillations were detected (sample 2) on the other hand. For sample 1, we estimate the percentages of false negative detections (i.e. the number of stars which we predict no seismic detection). For sample 2, we estimate the percentages of false positive detections (i.e. the number of stars from which we predict a seismic detection). For the results, we consider 3 types of mass regimes: R1 (MS stars with  $M < 1.6M_{\odot}$  and subgiants all masses), R2 (stars with  $M \leq 1.2$ ), R3 (MS stars with  $M \leq 1.2$ )

### B.1. Probability of detection for the sample 1 and sample 2

When computing the detection probability for sample 1 (413 stars), we assumed as our baseline the following input assumptions:  $\nu_{\max}$ ,  $\Delta\nu$  and  $T_{\text{eff}}$  are from M22, masses are derived with Eq.A.3 and  $\delta\nu_{\text{env}} = \nu_{\max}/2$ . The yields are listed in Table B.1. We find, in the R1 mass regime when  $P_{\text{det}} \leq 0.99$ , a percentage of about  $\sim 10\%$  of false negative detections when the detection probability is  $P_{\text{det}} \leq 0.99$  and  $\sim 5\%$  when  $P_{\text{det}} \leq 0.90$ .

The choice of  $P_{\text{det}} \leq 0.99$  obviously predicts a larger number of false negative detections compared to the choice of  $P_{\text{det}} \leq 0.90$  and is therefore more conservative for estimating the percentage of positive detections. As a sanity check, we verified that all stars in the Legacy sample are found with a detection probability equal to 1 as expected.

We next considered the 990 *Kepler* stars in sample 2. For that sample, we assumed as our baseline the following input assumptions:  $\nu_{\max}$  derived from  $\log g$  and  $T_{\text{eff}}$  given by M19,  $\Delta\nu$  from the scaling relation Eq.A.5 with  $a = 1$ ,  $s = 0.82$ , masses are derived with Eq.A.8 and  $\delta\nu_{\text{env}} = \nu_{\max}/2$ . Table B.2 provides the yields of the calculations of the detection probability for those stars. Assuming a seismic positive detection when  $P_{\text{det}} > 0.99$ , we find that the percentage of false positive detections is  $\sim 20\%$ ,  $11\%$ , and  $7\%$  for the R1, R2, and R3 mass regimes, respectively.

When smoothing the PSD in order to decrease the noise level in case of a low S/N, it is found that the measured amplitudes are decreased by about  $6\%$  compared to the true amplitudes

**Table B.1.** Numbers of false negative detections for sample 1 with known detected oscillations assuming the baseline conditions. Number of stars predicted with NO seismic detection. Masses in solar unit.

mass regime	R1	R2	R3
nb of stars	413 stars	276 stars	52 stars
$P_{\text{det}} \leq 0.90$	20 ~ 5%	9 ~ 3%	7 ~ 13%
$P_{\text{det}} \leq 0.99$	40 ~ 10%	16 ~ 6%	11 ~ 21%

**Table B.2.** Numbers of false positive detections for the stars of sample 2 assuming the baseline case for that sample. Numbers of stars predicted with seismic positive detection. Masses are in solar units.

mass regime	R1	R2	R3
nb of stars	936	396	361
$P_{\text{det}} > 0.90$	279 ~ 30%	64 ~ 16%	44 ~ 12%
$P_{\text{det}} > 0.99$	186 ~ 20%	44 ~ 11%	27 ~ 7%

(Lund et al. 2017). Assuming detection when  $P_{\text{det}} > 0.99$ , the impact of decreasing our theoretical amplitudes by 6% leads to a percentage of false positive detections ~ 17%, 10%, 6% for the R1, R2 and R3 mass regimes, respectively, which is slightly lower than for the baseline case (~ 21%, 11% and 7% in Table B.1). The impact is not important and we will no longer consider the case of decreasing the amplitudes. Here the choice of  $P_{\text{det}} > 0.99$  rather than 0.90 provides a lower number of false positive detections.

Hence, in both cases above,  $P_{\text{det}} > 0.99$  is the conservative choice, namely, lowering the number of positive detections and maximising the number of false detections. We therefore adopted a detection threshold at 99% when considering the PLATO targets.

There are a number of assumptions behind the above calculations which lead to some uncertainties in the results. In the next sections, we estimate the impact of the main sources of uncertainties in predicting the detection probability (assuming the conservative case of a detection threshold at 99%).

## B.2. Impact of uncertainties in the input quantities

We estimated the impact on the detection probability of the uncertainties in the various input quantities. We carried out the calculations, changing one or several input quantities at a time and the results must be compared to the results obtained with the baseline cases.

We assessed first the impact on the number of false negative detections with sample 1 when using the values of  $\nu_{\text{max}}$ ,  $\Delta\nu$ , and  $T_{\text{eff}}$  from the S17 instead of using those of M22. The results are listed in Table B.3. We note that the number of stars in each mass regime can change depending on the adopted assumptions, specifically because the seismic mass is computed using a scaling relation which involves  $\nu_{\text{max}}$ ,  $\Delta\nu$ , and  $T_{\text{eff}}$ . The false negative detections in case of the S17 input parameters are ~ 11%, 14%, 16% for R1, R2, and R3, respectively (Table B.3), namely, slightly greater than ~ 10%, 6%, and 21%, respectively, when using the set  $\nu_{\text{max}}$ ,  $\Delta\nu$  and  $T_{\text{eff}}$  from

**Table B.3.** False negative detections for sample 1. Each row corresponds to one change compared to the baseline case. Figures in parenthesis correspond to the total number of stars in each mass regimes and considered case. Masses,  $M$ , are in solar units.

mass regime	R1	R2	R3
$\nu_{\text{max},\text{S17}}$	44 (413) ~ 11%	19 (276) ~ 7%	17 (64) ~ 27%
$T_{\text{eff},\text{S17}}$	59 (413) ~ 14%	17 (224) ~ 8%	8 (50) ~ 16%
$(\nu_{\text{max}}, \Delta\nu$ & $T_{\text{eff}})_{\text{S17}}$	65 (413) ~ 16%	22 (224) ~ 10%	15 (53) ~ 28%
$\Delta\nu_{\text{scaling}}$	33 (413) ~ 8%	12 (276) ~ 4%	11 (52) ~ 21%
$\delta\nu_{\text{env}} = \nu_{\text{max}}$	14 (413) ~ 4%	6 (276) ~ 2%	5 (56) ~ 9%

**Table B.4.** False positive ( $P_{\text{det}} > 0.99$ ) for sample 2. The baseline is assumed except for  $\delta\nu_{\text{env}} = \nu_{\text{max}}$ . Masses,  $M$ , in solar unit.

mass regime	R1	R2	R3
	936	403	370
$\delta\nu_{\text{env}} = \nu_{\text{max}}$	316 34%	76 19%	54 16%

M22 in Table B.2. The impact is higher when considering the smaller sample of MS stars with  $M \leq 1.2$  (R3) than the whole sample (R1).

As a second type of uncertainty, we considered the changes when one uses the scaling relation Eq. (A.5) (with  $s = 0.82$  and  $a = 1$ ) for  $\Delta\nu$ ,  $\Delta\nu_{\text{scaling}}$ , which is what we have to use in absence of an observed value (case of sample 2 and Plato targets) in Appendix A. We computed the detection probability using our adopted sample of oscillating stars, sample 1. As can be seen from Table B.3, we find false negative detections at the level of 8%, 4%, and 21% for the R1, R2, and R3 mass regimes, respectively. These figures must be compared with 10%, 6%, and 21%, respectively found with the baseline case (Table B.2). Here the changes in the false negative percentages come from the fact that changing the values of  $\nu_{\text{max}}$  and  $\Delta\nu$  impacts the mass derived with the scaling relation Eq. (12) and, thus, the number of stars in each subsample. The impact remains small.

The third type of uncertainty concerns our choice for the width of the envelope of the oscillations in a power spectrum. We then compare the yields obtained assuming the baseline case  $\delta\nu_{\text{env}} = \nu_{\text{max}} = 1/2$  and the more optimist case  $\delta\nu_{\text{env}} = \nu_{\text{max}}$  for sample 1. In Table B.3, we can see that the false negative detections are about 2.5 smaller than when assuming  $\delta\nu_{\text{env}} = \nu_{\text{max}}/2$ . One then underestimates the detection rates when assuming  $\delta\nu_{\text{env}} = \nu_{\text{max}}$  compared to the  $\delta\nu_{\text{env}} = \nu_{\text{max}}/2$  case. The comparison between the two options for  $\delta\nu_{\text{env}}$  can also be made with sample 2 for the false positive detection rates. One finds a higher false positive detection rate when assuming  $\delta\nu_{\text{env}} = \nu_{\text{max}}$  (Table B.4) instead of  $\delta\nu_{\text{env}} = \nu_{\text{max}}/2$  (Table B.2). Therefore, we overestimate the positive detection rate when assuming  $\delta\nu_{\text{env}} = \nu_{\text{max}}$  compared with the  $\delta\nu_{\text{env}} = \nu_{\text{max}}/2$  case.

As a net result and to remain conservative, we chose the option which gives a lower false positive detection rate to the

**Table B.5.** Number of stars and associated percentages of predicted false negative and positive detections when considering the whole *Kepler* population with and without real detection in each regimes and the baseline assumptions. Masses,  $M$ , are in solar units.

mass regime	R1	R2	R3
nb of stars	1349	620	412
False negative	40 (~ 3%)	16 (~ 3%)	11 (~ 3%)
False positive	186 (~ 14%)	44 (~ 7%)	27 (~ 7%)

**Table B.6.** Number of stars and associated percentages of predicted false negative and positive detections when considering the whole *Kepler* population with and without real detection in each regimes and the baseline assumptions except for  $\delta v_{\text{env}} = v_{\text{max}}$ . Masses,  $M$ , are in solar units.

mass regime	R1	R2	R3
nb of stars	1349	679	426
False negative	14 (~ 1%)	6 (~ 0.9%)	5 (~ 1%)
False positive	326 (~ 24%)	76 (~ 11%)	54 (~ 13%)

cost of a higher false negative rate. This justifies taking  $\delta v_{\text{env}} = v_{\text{max}}/2$  for our baseline condition. We will nevertheless provide also the results in the more optimistic case  $\delta v_{\text{env}} = v_{\text{max}}$  for the PLATO targets.

### B.3. Global uncertainties for the predicted percentage of predicted seismic detection

In anticipation of the investigation for the PLATO case, we considered as a single sample the total sample of 1349 *Kepler* stars with detected solar-like oscillation (413 stars, sample 1) and with no detection of solar-like oscillation (936 stars from sample 2) in the R1 mass regime and similarly the total sample of 620 stars in the R2 mass regime and the total sample of 412 stars in the R3 mass sample.

According to Table B.5, the calculations predicting the number of seismic positive detections applied to PLATO targets in Sect. 5 underestimate it by 3.0% for all mass regimes and overestimate it by 14%, 7%, 7% for the R1, R2, and R3 mass regimes respectively in the baseline conditions. We then used those rates to estimate the uncertainties on the predicted number of positive detections, say  $X$ , for the PLATO targets in Sect.5, as follows:  $X_{-14\%}^{+3\%}$  for R1,  $X_{-7\%}^{+3\%}$  for R2, and  $X_{-7\%}^{+3\%}$  for R3.

Similar estimates assuming  $\delta v_{\text{env}} = v_{\text{max}}$  can be found in Table B.6.

## Appendix C: Uncertainties of the inferred mass, radius, and age

We seek relative uncertainties for the mass, radius, and age,  $\delta M/M$ ,  $\delta R/R$ ,  $\delta A/A$ , which can be computed for the PIC targets. In accordance with the stellar requirements of the PLATO mission (which is the most challenging goal), we focus exclusively on the MS stars with masses  $\leq 1.2M_{\odot}$ .

We want to estimate the purely statistical uncertainties for the seismically inferred masses, radii, and ages generated by the propagation of seismic observational uncertainties only. In order to eliminate as much as possible all systematic errors (which will be briefly discussed in the conclusions/discussion

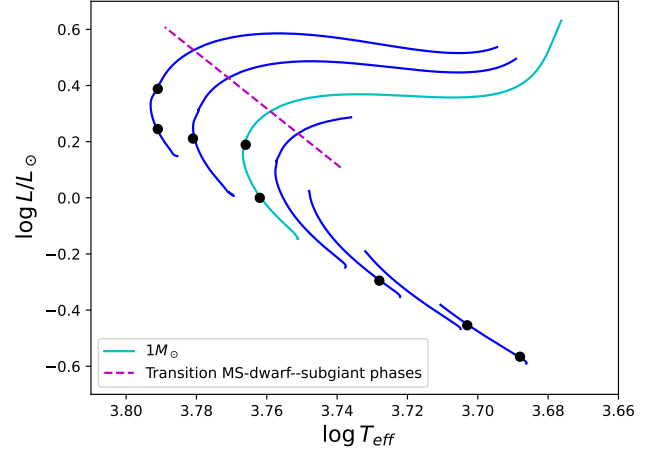


**Fig. C.1.** Evolutionary tracks for masses from 0.8 to  $1.15M_{\odot}$  in step of  $0.05M_{\odot}$  (blue solid curves) in a HR diagram. The black dots indicate the location of the synthetic target stars studied here. The magenta dashed line shows the location of models with their central hydrogen content  $X_c \sim 10^{-6}$  which we take here as the transition between MS stars and subgiant phases. The transition follows the empirical relation :  $\log L/L_{\odot} = 10(\log T_{\text{eff}} - 3.7532) + 0.25$  for that range of mass given the adopted chemical composition and physics of the stellar models.

section), we built a set of synthetic stars which masses and ages covering the ranges of interest here:  $(M/M_{\odot}, A(\text{Gyr})) = (0.9, 3.), (1.0, 2.), (1.0, 4.57), (1.0, 9.0), (1.03, 4.6), (1.08, 4.6), (1.15, 2.0), (1.15, 9.0)$  and infer their seismic masses, radii, and ages by means of a routinely used a grid-based approach, as described in Cunha et al. (2021).

### C.1. A set of synthetic stars and their frequencies

We built the stellar models of the synthetic stars with the evolutionary code CESTAM (Morel & Lebreton 2008; Marques et al. 2013) with the input physics as much as possible similar to that of the stellar models included in the input grid. The locations of those fictitious stars in the HR diagram are shown in Fig. C.1.

The frequencies for each synthetic star are calculated with ADIPLS (Christensen-Dalsgaard 2008). The adopted uncertainties on the frequencies are scaled with respect to those of the ‘degraded Sun’ (corresponding to the Sun seen as a star) (Lund et al. 2017) which was used as a reference for the studies of the *Kepler* Legacy sample in Silva Aguirre et al. (2017). For the degraded Sun, the  $\ell = 1$  mode frequency closest to  $v_{\text{max}}$  ( $v_{\text{max},\odot} = 3090\mu\text{Hz}$ ) with the smallest uncertainty ( $\delta v_{\ell=1, \text{max},\odot} = 0.057\mu\text{Hz}$ ) is  $v_{\ell=1, \text{max},\odot} = 2963.3\mu\text{Hz}$ .

For each synthetic star, the frequency uncertainty for each frequency  $v_{nl}$  is taken as  $\delta v_{n,\ell} = x \times \delta v_{n,\ell,\odot}$ . We infer the MRA uncertainties for the cases  $x = 1, 3, 5, 7, 10$ , which cover the range of uncertainties for the PLATO P1P2 sample.

For sake of simplicity, we keep the same number and types of modes as given above for which frequencies are computed in all considered cases, although this number decreases when the S/N decreases. Some impact of such degradation is discussed in Cunha et al. (2021).

### C.2. MRA inference for the set of synthetic stars

The stellar MRA and their uncertainties are obtained with the inference code AIMS (Rendle et al. 2019; Lund & Reese 2018). AIMS reads as an input a precomputed grid of stellar models.

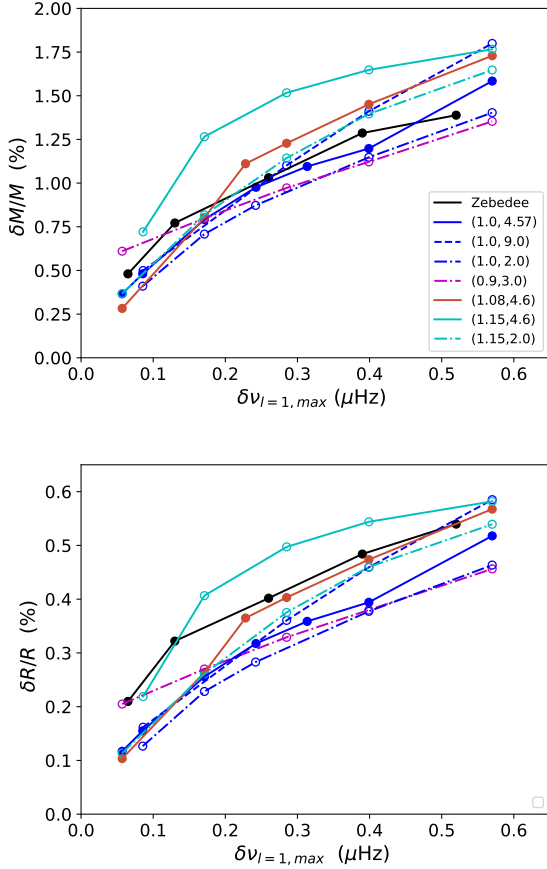


**Fig. C.2.** Relative uncertainties for the masses (top) and radii (bottom) with increasing frequency uncertainties for all synthetic stars as a function of  $\delta\nu_{\ell=1,\max}$ . The color code is given in the panels as  $(M/M_{\odot}, \text{age (Gyr)})$ . The solid blue corresponds to a Sun. The solid curve with black dots represents a case similar to Zebedee ( $1.0165 M_{\odot}$ ,  $3.085$  Gyr) in Cunha et al. (2021).

For convenience, we adopt the stellar grid described and used in Cunha et al. (2021).

The observational constraints for each star are  $T_{\text{eff}}, L/L_{\odot}, [Fe/H]$ , and the frequencies of the individual modes  $\ell = 0$  ( $n = 16 - 27$ ),  $1$  ( $n = 16 - 27$ ),  $2$  ( $n = 15 - 27$ ) for the degree  $\ell$  and radial order  $n$  similar to the synthetic star known as Zebedee (a young Sun) studied in Cunha et al. (2021). In order to eliminate systematic errors that are not relevant in this section, we take as central values the exact values of  $T_{\text{eff}}, L/L_{\odot}, [Fe/H]$  from the models of the synthetic stars. The uncertainties ( $1\sigma$ ) adopted are  $70K, 0.3, 0.05$  respectively, as expected at the time of PLATO launch.

For comparison with the results in Cunha et al. (2021), we also inferred the stellar mass, radius, and age, and their uncertainties for the Zebedee case (real values of the corresponding stellar model:  $M/M_{\odot}, A(\text{Gyr}) = 1.0165, 3.085$ ). In that particular case, the uncertainties are taken from Cunha et al. (2021). Since the input frequencies for that synthetic star included surface-effect corrections according to the formulation of Ball & Gizon (2014a,b), we also included the surface effect correction according to the same prescription when inferring the stellar parameters for Zebedee with the AIMS code. The results compare well with the results published in Cunha et al. (2021) and we do not show them.

The variations of the relative uncertainties for the inferred mass, radius, and age are shown as a function of the uncertain-

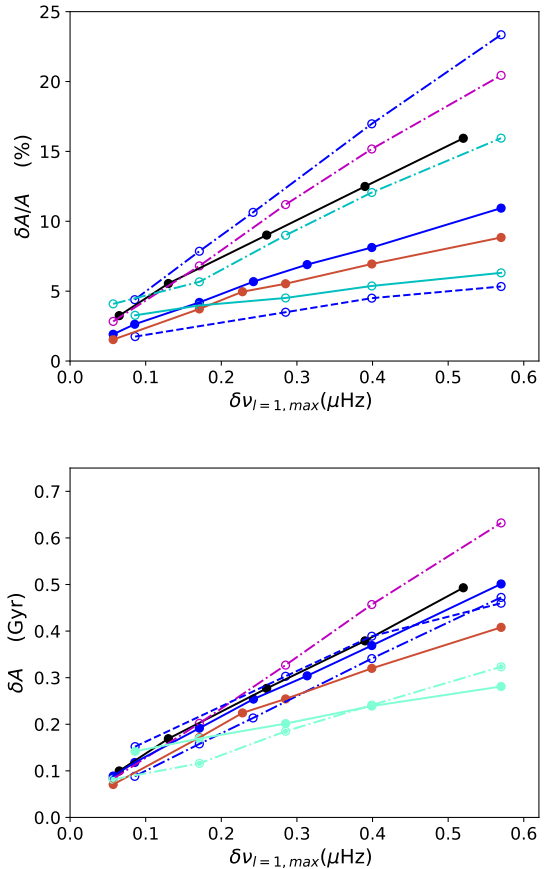


**Fig. C.3.** Same as in Fig. C.2 but for the age uncertainties (top: relative, bottom: absolute).

ties  $\delta\nu_{\ell=1,\max}$  in Figs. C.2 and C.3. As expected the MRA uncertainties increase with increasing  $\delta\nu_{\ell=1,\max}$ . It can be seen that the precision for the inferred mass and radius is so high that a comfortable margin is left for systematic errors that must be added quadratically in order to obtain realistic mass and radius uncertainties while still satisfying the PLATO requirements. This is also true of stars like the Sun (in mass and age). Indeed for such a Sun-like star, with a frequency uncertainty  $\delta\nu_{\ell=1,\max} = 0.2\mu\text{Hz}$ , the relative age uncertainty is below 5%.

In view of application to the PLATO samples in Sect. 6, we show the same results in Fig. C.4 than in Fig. C.2 and Fig. C.3, respectively, but without the mass and age information. We then carried out linear fits of the general trends for the mass and radius uncertainties. For the mass and radius relative uncertainties (in %), the fits give:

$$\begin{cases} \delta M/M = 2.083 \delta\nu_{\ell=1,\max} + 0.046 \\ \delta R/R = 0.707 \delta\nu_{\ell=1,\max} + 0.149 \end{cases}, \quad (\text{C.1})$$

where  $\delta\nu_{\ell=1,\max}$  is in  $\mu\text{Hz}$ . The above relations are used for the PIC targets in Sect. 5. The scatter (about 0.5% and 0.1% for the the mass and radius relative uncertainties, respectively) due to different masses and ages remains acceptable for our purposes.

We also see that there is too large a scatter for enabling a meaningful fit for  $\delta A/A$ . This would be possible for the absolute age uncertainty,  $\delta A$ . We actually found

$$\delta A = 0.702 \delta\nu_{\ell=1,\max} + 0.054, \quad (\text{C.2})$$

but for the PIC targets, the age is unknown and we can only use the relative age uncertainty so we will rather adopt an

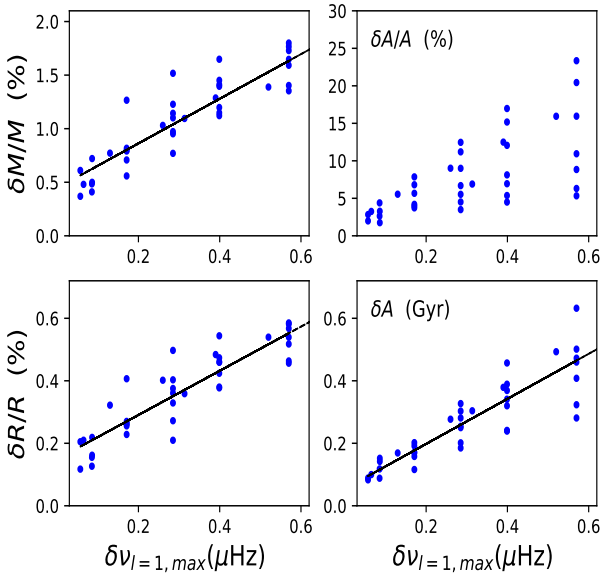


**Fig. C.4.** Uncertainties for all synthetic stars (blue dots). Solid black curve: linear fits (see text).

alternative criterion. As shown in Fig. C.4 for  $\delta A/A$ , the relative statistical uncertainty amounts roughly to 7% when  $\delta\nu_{\ell=1, \text{Libb}, \nu_{\text{max}}} < 0.2 \mu\text{Hz}$ . We then adopt the criterion:

$$\delta\nu_{\ell=1, \text{Libb}, \nu_{\text{max}}} < 0.2 \mu\text{Hz}, \quad (\text{C.3})$$

to select the cases for which relative age uncertainties of  $< 10\%$  can be expected. This is in accordance with Appourchaux (2020). This leaves as much margin to allow for systematic errors (that must be added in quadrature to obtain the final uncertainties). This is a challenge that has driven -and still drives- many theoretical studies in the community (see Sect. 7 for a brief discussion).

## Appendix D: Relation between $\sigma_{\text{Libb}, \ell=1}$ and

$$\delta\nu_{\ell=1, \text{max}}$$

In absence of observations as it is the case today for the PLATO targets, a convenient way of estimating the uncertainties of individual frequencies of solar-like oscillation mode is the generally accepted Libbrecht (1992) relation:

$$\sigma_{\text{Libb}}^2 = f(\beta) \frac{\Gamma}{4\pi T_{\text{obs}}} \quad (\text{D.1})$$

with

$$f(\beta) = (1 + \beta)^{1/2} \left[ (1 + \beta)^{1/2} + \beta^{1/2} \right]^3 \quad (\text{D.2})$$

where  $\beta = 1/(S/N)$  is the inverse of the S/N,  $\Gamma$  (in  $s^{-1}$ ) is the FWHM linewidth of the mode, and  $T_{\text{obs}}$  (in s) the duration of the observation. It is well accepted that this statistical estimate of the frequency uncertainties of solar-like oscillation modes represents well the reality.

To proceed further, we denote  $\sigma_{\text{Libb}, \ell=1, \text{max}}$  the Libbrecht (1992) frequency uncertainty on the frequency of a  $\ell = 1$  mode closest to  $\nu_{\text{max}}$ . It is evaluated for each star with  $(S/N)_{\text{max}}$  given by Eq. (8) and  $\Gamma$  in Table D.1 below.

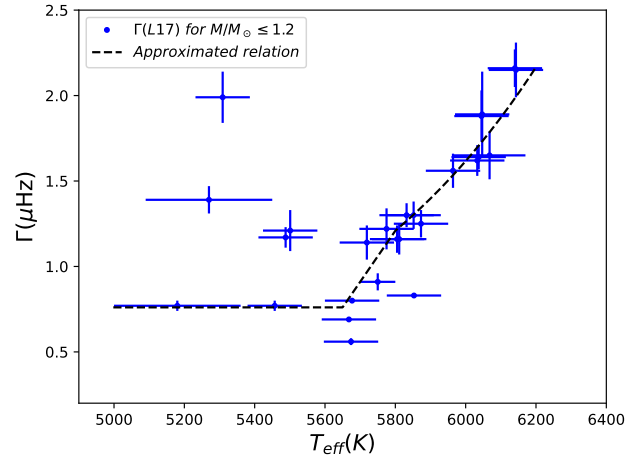


**Fig. D.1.** Variation of  $\Gamma$  with the effective temperature. Blue crosses are the observed values while the dashed line represents the computed  $\Gamma$  values.

**Table D.1.** Empirical relation for the linewidth  $\Gamma_{\ell=1, \text{max}}$  derived from a fit of the Lund et al. (2017)'s data (Fig. D.1).

$T_{\text{eff}}$ (K)	$\Gamma_{\ell=1, \text{max}}$
[5800, 6400]	$0.2 + 0.97 (T_{\text{eff}}/T_{\text{eff}, \odot})^{10}$
[5650, 5800]	$0.76 + 17.3 (T_{\text{eff}} - 5600)/T_{\text{eff}, \odot}$
[4900, 5650]	$\Gamma_0 = 0.76$

### D.1. Deriving $\Gamma_{\ell=1, \text{max}}$ for estimating $\sigma_{\text{Libb}, \ell=1, \text{max}}$

For each star, we take from Lund et al. (2017) the values of the linewidth,  $\Gamma_{\ell=1, \text{max}}$ , of the  $\ell = 1$  mode with the frequency closest to  $\nu_{\text{max}}$ . Those values are represented in Fig. D.1 as function of the effective temperature. We restrict the case to P1P2 stars with mass  $\leq 1.2M_{\odot}$  which are the PLATO targets for which we will estimate the MRA uncertainties in Sect. 6. One clearly notes two regimes: one regime at high effective temperature where  $\Gamma_{\ell=1, \text{max}}$  increases almost linearly with the effective temperature and one regime at low effective temperature where the scatter and the large uncertainties prevent from establishing a trend with  $T_{\text{eff}}$ . In the low regime, we therefore keep  $\Gamma_{\ell=1, \text{max}}$  constant at the lowest value  $\Gamma_0$  and consider also the case when  $3\Gamma_0$  for  $T_{\text{eff}} \leq 5650$  K (Fig. D.1). We then adopt for  $\Gamma_{\ell=1, \text{max}}$  (in  $\mu\text{Hz}$ ) the scaling relation adapted from Appourchaux et al. (2012) (Table 2) and given in Table D.1.

### D.2. Converting $\sigma_{\text{Libb}, \ell=1, \text{max}}$ to $\delta\nu_{\ell=1, \text{max}}$

Using Kepler LEGACY data, we have derived in Appendix C the MRA uncertainty as a function of the observed individual frequency uncertainty,  $\delta\nu_{\text{max}}$ . We then need to convert  $\sigma_{\text{Libb}, \ell=1, \text{max}}$  into the frequency uncertainty  $\delta\nu_{\ell=1, \text{max}}$ . Again here we use the Kepler Legacy data to carry out that calibration.

For each star, Fig. D.2 displays the ratio  $\delta\nu_{\ell=1, \text{max}}/\sigma_{\text{Libb}, \ell=1, \text{max}}$  as a function of the effective temperature. There is a clear trend: the ratio decreases with the effective temperature. For convenience, we derive a linear fit to represent that trend about that fit. The linear fit gives:

$$\frac{\delta\nu_{\ell=1, \text{max}}}{\sigma_{\text{Libb}, \ell=1, \text{max}}} = 4.89 - 4.18 \frac{T_{\text{eff}}}{6000\text{K}} \quad (\text{D.3})$$

valid for  $5000 < T_{\text{eff}} \leq 6200 \text{ K}$ . The scatter about the linear relation is about  $\pm 0.5$ . In Sect.6.2, we will therefore consider the effect of adding  $\sim 0.5$  to the above linear relation on the results for the PLATO targets.

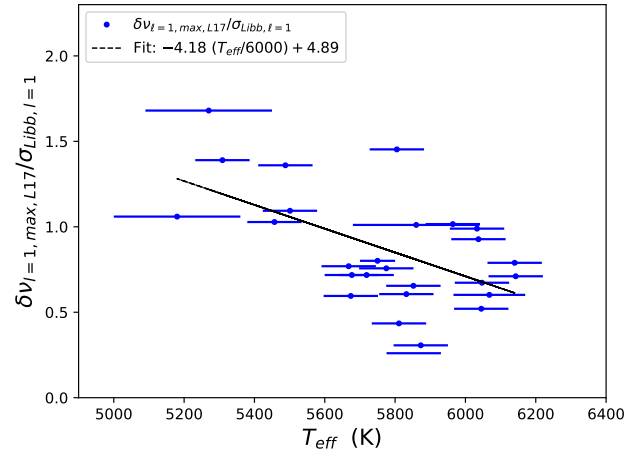


**Fig. D.2.** Variation of the ratio  $\delta \nu_{l=1, \text{max}} / \sigma_{\text{Libb}}$  with the effective temperature (blue crosses). The black curve is a linear fit.